

Transferring Information from CFD to FE Thermal Analysis

Application to a cooling film

Master's thesis in Master Programme Sustainable Energy Systems

Felix Larsson

MASTER'S THESIS 2016:35

Transferring Information from CFD to FE Thermal Analysis

Application to a cooling film

Felix Larsson



CHALMERS
UNIVERSITY OF TECHNOLOGY

Department of Applied Mechanics
Division of Fluid Dynamics
CHALMERS UNIVERSITY OF TECHNOLOGY
Gothenburg, Sweden 2016

Transferring Information from CFD to FE Thermal Analysis
Application to a cooling film
Felix Larsson

© Felix Larsson, 2016.

Supervisors: Andreas Fahlvik Svensson, GKN Aerospace
Linus Marstorp, GKN Aerospace
Examiner: Lars Davidsson, Department of Applied Mechanics

Master's Thesis 2016:35
Department of Applied Mechanics
Division of Fluid Dynamics
Chalmers University of Technology
SE-412 96 Gothenburg
Telephone +46 31 772 1000

Cover: A turbine rear structure.

Typeset in L^AT_EX
Printed by [Name of printing company]
Gothenburg, Sweden 2016

Transferring Information from CFD to FE Thermal Analysis
Application to a cooling film
Felix Larsson
Department of Applied Mechanics
Chalmers University of Technology

Abstract

This Master's Thesis was conducted at GKN Aerospace, Trollhättan. In this project different one way coupling procedures between computational fluid dynamics (CFD) and finite element analysis (FEA) has been evaluated. A method using 1D thermal loads for the structural simulations was compared a newly proposed method using 2D Thermal loads. Two inhouse codes *BCgen2* and *BCgen_2D_mapping* from GKN Aerospace were used to supply thermal loads of one and two dimensions respectively. Conjugated CFD was used as reference in both case one and case two.

As a first case a 2D boundary layer was simulated in ANSYS® Fluent® which demonstrated the importance of the choice of reference temperature. The results shows that the most appropriate temperature was the adiabatic wall temperature.

The second case included a turbine cascade geometry in three dimensions modified to include a leak flow slot and a strut fillet radius. The use of thermal loads of two dimensions on the hub surface proved to result in superior temperature predictions compared to the 1D method. The methods were also applied to an existing turbine rear structure geometry. Details of the hot wake area as well as temperature difference in the hub region closest to the vane, resolved using 2D thermal loads, resulted in significant differences in the level of material stresses predicted compared to the ones given using 1D thermal loads.

Keywords: one-way coupling, CFD, FE, Thermal Analysis, Boundary condition

Acknowledgements

To start with, I would like to express my sincere gratitude towards my supervisors at GKN Aerospace, Andreas Fahlvik Svensson and Linus Marstorp for their great support during this project. Without your support this project would have been impossible to pursue. I would also like to thank my examiner Lars Davidson for his valuable inputs and my coworkers who provided aid when necessary and contributed to the very welcoming atmosphere at the company.

Felix Larsson, Gothenburg, June 2016

Contents

| | |
|---|-------------|
| List of Figures | xiii |
| List of Tables | xv |
| 1 Introduction | 1 |
| 1.1 Project scope | 1 |
| 2 Theory | 3 |
| 2.1 Gas turbines | 3 |
| 2.2 Convective heat transfer | 4 |
| 2.3 Computational fluid dynamics | 4 |
| 2.3.1 Governing equations | 5 |
| 2.3.2 Reynold averaged Navier-Stokes equation | 5 |
| 2.3.3 Realizable k- ϵ -model | 6 |
| 2.4 Finite element method | 7 |
| 2.4.1 Derivation of the Fourier partial differential equation | 7 |
| 2.4.2 Derivation of the equation system in 1D | 7 |
| 2.4.3 Solution procedure | 8 |
| 2.5 Coupling procedure | 11 |
| 2.5.1 One dimensional correlation | 11 |
| 2.5.2 BCgen2 | 11 |
| 2.5.3 BCgen_2D_mapping | 11 |
| 2.5.4 Conjugated CFD | 11 |
| 2.6 Frössling correlation | 11 |
| 3 Methods | 13 |
| 3.1 2D boundary layer | 13 |
| 3.1.1 Mesh and settings | 13 |
| 3.2 Hub film | 15 |
| 3.2.1 Mesh test and sensitivity analysis | 16 |
| 3.2.2 Testing of the method | 17 |
| 4 Results | 19 |
| 4.1 2D boundary layer | 19 |
| 4.1.1 Mesh test | 19 |
| 4.1.2 Inlet boundary conditions | 19 |
| 4.1.3 Wall temperature dependence | 20 |

| | | |
|----------|---|-----------|
| 4.1.4 | Steady state simulations | 20 |
| 4.2 | Hub film | 24 |
| 4.2.1 | Mesh test | 24 |
| 4.2.2 | Sensitivity analysis for inlet and wall temperature | 24 |
| 4.2.3 | Structural temperature profiles | 27 |
| 4.2.4 | Real case | 38 |
| 5 | Conclusion | 41 |
| 5.1 | Future work | 41 |
| | Bibliography | 43 |
| A | Appendix 1 - Transient simulations | I |

Nomenclature

Abbreviations

| | |
|-----|------------------------------|
| CFD | Computational fluid dynamics |
| FE | Finite Element |
| FEA | Finite Element Analysis |
| HTC | Heat Transfer Coefficient |
| ps | Pressure side |
| ss | Suction side |

Greek symbols

| Variable | Description | Unit |
|-------------|------------------------------|-----------|
| ρ | Density | kg/m^3 |
| μ | Dynamic viscosity | $kg/(ms)$ |
| ν | Kinematic viscosity | m^2/s |
| ν_T | Eddy viscosity | m^2/s |
| τ_{ij} | Shear stress | Pa |
| ϵ | Turbulent dissipation rate | m^2/s^3 |
| λ | Thermal conductivity | $W/(mK)$ |
| α | Temperature ramp coefficient | – |
| η | Mixing factor | – |

Roman symbols

| Variable | Description | Unit |
|----------------|--------------------------------|----------|
| a | Time of working point change | s |
| t | Time | s |
| U | Velocity | m/s |
| P | Pressures | Pa |
| i | Internal energy | J |
| k | Konductivity | $W/(mK)$ |
| q | Heat flux | W |
| V | Volume | m^3 |
| T_{ref} | Referens temperature | K |
| $T_{wall}&T_w$ | Wall Temperature | K |
| T_1 | Leak flow total temperature | K |
| T_2 | Inlet total bulk temperature | K |
| T_{bulk} | Fluid Temperature at wall | K |
| T_{static} | Static inlet fluid temperature | K |
| T_{total} | Total inlet bulk temperature | K |
| v | Velocity | m/s |
| ΔT | Temperature difference | K |

Dimensionless numbers

| Variable | Description | Definition |
|----------|-------------|------------|
|----------|-------------|------------|

Contents

| | | |
|--------|---------------------------|-----------------------|
| Nu_x | The local Nusselts number | $\frac{hL}{k}$ |
| Re_x | The local Reynolds number | $\frac{\rho vx}{\mu}$ |
| Pr | The Prandtl number | $\frac{C_p \mu}{k}$ |

List of Figures

| | | |
|------|---|----|
| 2.1 | The figure shows a two shaft turbofan. Multiple shafts increases efficiency by offering two different rotational velocities instead of one. Also note the bypass flow around the core engine which further increases the engine efficiency and reduces noise levels. | 4 |
| 3.1 | Mesh used in the 2D-Duct case. The points marks the edges of the wall. | 14 |
| 3.2 | The cascade geometry used in the simulations. | 16 |
| 4.1 | Mesh sensitivity analysis. Comparison of wall fluxes using meshes A-D. | 20 |
| 4.2 | Comparison between different inlet conditions specified in table 3.2. . | 21 |
| 4.3 | Comparison of resulting HTC's using different fixed wall temperatures. | 21 |
| 4.4 | Metal wall temperatures resulting from different methods. In the adiabatic cases has an adiabatic cfd simulation been performed to calculate the fluid temperature at the wall temperature. An area weighted average of 816.34 K was used as reference temperature in these cases. Otherwise the inlet bulk temperature of 840 K was used . | 22 |
| 4.5 | Wall temperature as a function of the reference temperature. | 23 |
| 4.6 | Meshtest of three different meshes (a-c) and sensitivity analysis for wall temeprature (d-f). | 25 |
| 4.7 | Sensitivity analysis for inlet temperature. | 26 |
| 4.8 | Resulting wall temperatures using 1D blade fields with varying hub fields | 28 |
| 4.9 | Resulting wall temperatures using 2D blade fields with varying hub fields | 29 |
| 4.10 | Resulting pressure side blade wall temperatures using 1D blade fields with varying hub fields | 30 |
| 4.11 | Resulting suction side blade wall temperatures using 1D blade fields with varying hub fields | 31 |
| 4.12 | Comparison between 1D and 2D htc blade fields' effect on blade surface temperature with 2D hub field | 32 |
| 4.13 | Applied thermal loads of different resolutions. | 33 |
| 4.14 | Resolution effect investigation of the loads applied to the hub surface. Blade thermal loads are kept at 1D. | 34 |
| 4.15 | Effect of applying the Frössling correlation to the leading edge | 35 |
| 4.16 | Effect of applying the Frössling correlation to the leading edge, pressure side | 36 |

| | | |
|------|---|-----|
| 4.17 | Effect of applying the Frössling correlation to the leading edge, suction side | 37 |
| 4.18 | Contours of wall temperature using 1D and 2D thermal loads | 38 |
| 4.19 | Contours of von Mises Stresses using 1D and 2D thermal loads | 38 |
| A.1 | Wall temperature response to a linear total gauge pressure increase from 604 Pa to 16080 Pa over 10 seconds starting at time 0.01 s. Values are shown for three points on the wall surface. | II |
| A.2 | Wall temperature response to a total temperature increase from 800 K to 840 over 10 seconds starting at time 0.01 s. Values are shown for three points on the wall surface. | III |

List of Tables

| | | |
|-----|---|----|
| 3.1 | The different meshes tested | 14 |
| 3.2 | Inlet parameter setups tested | 15 |
| 4.1 | Quality of Mesh D | 19 |
| 4.2 | Point values taken at critical positions on the vane and hub surfaces . | 39 |

1

Introduction

For the majority of the engine parts the GKN Aerospace produces it is important to be able to predict the thermal environment accurately. The thermal profile of the component is often the main challenge during design and for this reason numerous initiatives are made to improve the computational methods used within the company.

The prediction of the thermal environment can be made through simple correlations derived from experimental data or it can be predicted using Computational Fluid Dynamics (CFD). This work has focused on so called non-coupled CFD-FE or one way coupled CFD-FE thermal analyses. As the fully coupled option resolves the 3D (or 2D) field of the fluid in every structural (Finite element, FE) time step the non-coupled procedure is based on CFD simulations made in key operating points. This simplification dramatically reduces the computational demand from a timescale of weeks to one in hours, but at the expense of accuracy. [16]

This thesis aimed at comparing an existing method to transfer information from CFD to FE thermal analyses as 1D fields with a newly proposed method using 2D fields.

Two cases has been examined of which the first one was a 2D-case and the second included two 3D geometries. The 2D-case consisted of a simple flat plate case where the boundary layer was resolved. The heat transfer through the wall was examined and used to calculate the resulting wall temperature profile using ANSYS® Mechanical. The second case consisted of a guide vane with a leakflow emerging from the hub surface prior to the blade. The first geometry was a modified cascade geometry while the second was a vane section from an existing turbine rear structure.

1.1 Project scope

The project was limited to only include one turbulence model. Further, no measurements were done within this project and conjugated CFD simulations were instead used as reference cases. Aside from the conjugated analysis, only one way coupling procedures were examined.

The project was limited to include three different structures; one geometry focusing on a boundary layer in two dimensions, one case using the existing cascade geometry from Chalmers University of Technology, and lastly a real turbine rear structure. The geometry and both the CFD and the structural meshes were created for the first case while in the second, modification were done on an existing geometry before mesh creation. For the last case, existing geometries, CFD and structural meshes, were used and focus was put on the simulation results from using

1. Introduction

the different coupling procedures examined.

2

Theory

Since the applications examined in this project are all gas turbine components a brief introduction to the concept is here included. Further the basics of computational fluid dynamics, finite element simulations and the coupling procedures are presented in this chapter.

2.1 Gas turbines

A gas turbine is a machine running according to the Brayton cycle and includes the steps compression, heat addition and expansion. The dominating way of adding heat to the system is by injection of a fuel such as natural gas or vaporized kerosene into a combustion chamber where it releases its chemically stored energy as heat during incineration. The heated air is then expanded through a turbine which is mounted on the same shaft as the compressor to supply the work required to compress the air. A net amount of work can then be harvested either as thrust as in aero engines or as work in a free turbine driving a generator for power production. It can be showed that the Brayton cycle has a higher efficiency for higher pressure ratios and for higher temperature levels for heat addition. This results in that all producers of gas turbines constantly looks for new materials and technologies to construct engines that are able to handle higher and higher temperatures without risking engine failures. The engines are also not allowed to emit excessive amounts of NO_x which is a large problem at higher temperatures where the nitrogen in the air reacts with oxygen. This is especially a problem for aero engines since there is no possibility of applying cleaning equipment of the exhausts without dramatically increasing the weight and thereby reducing the efficiency of the whole aircraft. An engine failure could potentially result in devastating consequences and must be avoided at all cost.

GKN Aerospace produces amongst other components the turbine rear structure (Front page) for several different aero engines. The turbine rear casing is the last step before the exhaust nozzles and therefore it steers the flow into a purely axial motion to make the most out of the fluid momentum. The component is exposed to high thermal stresses and it is crucial that it is appropriately designed since it also holds both the rear bearings to the turbine shafts and the rear engine attachment to the wing.

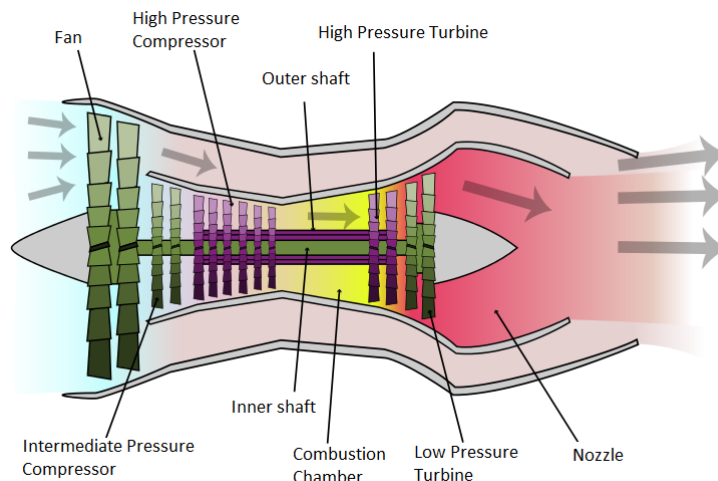


Figure 2.1: The figure shows a two shaft turbofan. Multiple shafts increases efficiency by offering two different rotational velocities instead of one. Also note the bypass flow around the core engine which further increases the engine efficiency and reduces noise levels.

2.2 Convective heat transfer

Convective heat transfer is the exchange of energy between a solid and the adjacent fluid. Newton described this phenomena using the following equation:

$$\frac{q}{A} = h\Delta T \quad (2.1)$$

Where q is the heat flux, A the area, h the heat transfer coefficient and T the temperature. In this thesis q/A is merged into simply writing q .

There always exists a region in the boundary layer closest to the wall where viscous effects are large. The thickness of this layer greatly affects the value of the heat transfer coefficient, sometimes also called the film coefficient. [15]

2.3 Computational fluid dynamics

Computational fluid dynamics (CFD) is a computer-based method of describing fluid motion, heat-transfer, and other phenomenas such as chemical reactions, which is steadily growing in importance. The development is closely coupled with the rapidly decreasing cost of computational power as the more effective machines decreases computational times and allows for higher resolution and more detailed results within reasonable time scales. This offers an attractive alternative or complement to the classic method of performing experiments. Except reducing the need for model testing CFD also offers a solution in every node of the domain while measurements are impossible to take at some locations. Thanks to these benefits many industries today perform CFD analyses routinely to calculate drag forces and other important parameters used in the development of their products.[14]

The base of the method is an equation system containing balances of momentum, energy and an equation ensuring continuity in the flow. Before solving the equation system the calculation domain has to be discretized into smaller elements over which the discretized equations are solved in an iterative manner. Also boundary conditions are required to make the system solvable with one unique solution. In theory the system can now be solved but in reality the extreme amounts of information together with the huge computational power required forces us to make simplifications which in turn demands models to close the equation system to make it solvable. These simplifications allow the system to be solved without resolving everything down to the smallest turbulent scales and these models can dramatically reduce the computational demand at the cost of the quality of the results. For most applications an exact solution is not necessary and the quality is still good enough.

2.3.1 Governing equations

Equations 2.2 to 2.7 are the governing equations for CFD simulations as given by H. K. Versteeg and W. Malalasekera [14].

$$\text{Continuity} \quad \frac{\partial \rho}{\partial t} + \text{div}(\rho \mathbf{u}) = 0 \quad (2.2)$$

$$\text{x-momentum} \quad \frac{\partial(\rho \mathbf{u})}{\partial t} + \text{div}(\rho \mathbf{u} \mathbf{u}) = -\frac{\partial p}{\partial x} + \text{div}(\mu \text{grad } u) + S_{Mx} \quad (2.3)$$

$$\text{y-momentum} \quad \frac{\partial(\rho \mathbf{u})}{\partial t} + \text{div}(\rho \mathbf{u} \mathbf{u}) = -\frac{\partial p}{\partial x} + \text{div}(\mu \text{grad } u) + S_{Mx} \quad (2.4)$$

$$\text{z-momentum} \quad \frac{\partial(\rho \mathbf{u})}{\partial t} + \text{div}(\rho \mathbf{u} \mathbf{u}) = -\frac{\partial p}{\partial x} + \text{div}(\mu \text{grad } u) + S_{Mx} \quad (2.5)$$

$$\text{Energy} \quad \frac{\partial(\rho i)}{\partial t} + \text{div}(\rho i \mathbf{u}) = -p \text{div}(\mathbf{u}) + \text{div}(k \text{grad } T) + \Phi + S_i \quad (2.6)$$

$$\text{Equations of state} \quad p = p(\rho, T) \text{ and } i = i(\rho, T) \quad (2.7)$$

Equation 2.2, also called the continuity equations is a mass balance over each computational cell which guarantees a physical mass flow throughout our domain. Equations 2.3 to 2.5 describe the forces acting on our cell while equation 2.6 is an energy balance. These last four equations can all be seen to contain a source term which production of each entity. Equation 2.6 also contains the dissipation term Φ . The equations of state relate the density and temperature to the pressure and internal energy.

2.3.2 Reynold averaged Navier-Stokes equation

As mentioned above the equations have to be simplified to fit for routine simulations. One common way proposed by Osborne Reynolds during the late 19th century was to divide instantaneous variables into a mean part and a fluctuating part.

$$U_i = \langle U_i \rangle + u_i \text{ and } P_i = \langle P_i \rangle + p_i \quad (2.8)$$

The momentum equations on this form are also called the Navier-Stokes equations. By dividing the instantaneous variables Reynold derived the so called Reynold averaged Navier-Stokes (RANS) equation of the form

$$\frac{\partial \langle U_i \rangle}{\partial t} + \langle U_j \rangle \frac{\partial \langle U_i \rangle}{\partial x_j} = -\frac{1}{\rho} \frac{\partial}{\partial x_j} \left\{ \langle P \rangle \delta_{ij} + \mu \left(\frac{\partial \langle U_i \rangle}{\partial x_j} + \frac{\partial \langle U_j \rangle}{\partial x_i} \right) - \rho \langle u_i u_j \rangle \right\} \quad (2.9)$$

where the important last term on the right hand side is known as the Reynold stress term. This term provides a coupling between the mean and the fluctuating parts of the velocity field but has to be modeled to close the equation system since the fluctuations are unknown. Hence the reduction of the data amounts generates a requirement of models to cover parts of the physics of the system. [1]

2.3.3 Realizable k- ϵ -model

There are many ways to model the Reynold stresses. One of the most popular ways is to relate the stresses to a dependent variable as is done in the so called Boussinesq approximation where the Reynold stresses are related to the mean velocity.

$$\frac{\tau_{ij}}{\rho} = -\langle u_i u_j \rangle = \nu_T \left(\frac{\partial \langle U_i \rangle}{\partial x_j} + \frac{\partial \langle U_j \rangle}{\partial x_i} \right) - \frac{2}{3} k \delta_{ij} \quad (2.10)$$

k is the turbulent kinetic energy per unit mass defined as $k = \frac{\langle u_i u_i \rangle}{2}$ and ν_T is a turbulent viscosity also called eddy viscosity introduced in the Boussinesq approximation.

Inserting this approximation into equation 2.9 results in

$$\begin{aligned} \frac{\partial \langle U_i \rangle}{\partial t} + \langle U_j \rangle \frac{\partial \langle U_i \rangle}{\partial x_j} = & -\frac{1}{\rho} \frac{\partial \langle P \rangle}{\partial x_i} - \frac{2}{3} \frac{\partial k}{\partial x_i} \\ & + \frac{\partial}{\partial x_j} \left\{ (\nu + \nu_T) \left(\frac{\partial \langle U_i \rangle}{\partial x_j} + \frac{\partial \langle U_j \rangle}{\partial x_i} \right) \right\} \end{aligned} \quad (2.11)$$

as presented by [1].

The Realizable k- ϵ model, which is a so called two equation model, calculates the eddy viscosity as

$$\nu_T = C_\mu \frac{k^2}{\epsilon} \quad (2.12)$$

where C_μ is a coefficient, k is the turbulent kinetic energy and ϵ is the turbulent dissipation rate. The model also introduces two transport equations to solve for k and ϵ which requires further assumptions. In comparison to the standard k- ϵ model the realizable k- ϵ defines the coefficient C_μ as a function instead of as a constant to guarantee that no unphysical negative normal stresses occur in the simulations. This should improve the models ability to describe rotating and separating flows.

2.4 Finite element method

2.4.1 Derivation of the Fourier partial differential equation

Define a cube of volume $dV = dx dy dz$. Using first order Taylor expansion

$$\dot{q}_{k+dk} = \dot{q}_k + \frac{\delta \dot{q}_k}{\delta k} dk \quad k=x,y,z \quad (2.13)$$

This can be written as

$$\begin{aligned} (\dot{q}_x - \dot{q}_{x+dx}) dy dz &= -\frac{\delta \dot{q}_x}{\delta x} dx dy dz = -\frac{\delta \dot{q}_x}{\delta x} dV \\ (\dot{q}_y - \dot{q}_{y+dy}) dx dz &= -\frac{\delta \dot{q}_y}{\delta y} dx dy dz = -\frac{\delta \dot{q}_y}{\delta y} dV \\ (\dot{q}_z - \dot{q}_{z+dz}) dx dy &= -\frac{\delta \dot{q}_z}{\delta z} dx dy dz = -\frac{\delta \dot{q}_z}{\delta z} dV \end{aligned} \quad (2.14)$$

The Fourier's law gives $\dot{q} = -\lambda \nabla T$ where λ is the thermal conductivity of the material. Inserting Fourier's law for q and adding the contribution from each dimension yields

$$\dot{Q}_{net} = \frac{\delta}{\delta x} \left(\lambda \frac{\delta T}{\delta x} \right) dV + \frac{\delta}{\delta y} \left(\lambda \frac{\delta T}{\delta y} \right) dV + \frac{\delta}{\delta z} \left(\lambda \frac{\delta T}{\delta z} \right) dV = \text{div}(\lambda \nabla T) dV \quad (2.15)$$

No heat sources or sinks are present and therefore

$$\dot{Q}_{net} = \text{div}(\lambda \nabla T) dV = \rho C_p \frac{\delta T}{\delta t} \quad (2.16)$$

which is Fourier's PDE. [9]

2.4.2 Derivation of the equation system in 1D

$$-(au_x)_x = f(x), x \in I = (0, l) \quad (2.17a)$$

$$au_x(0) = \kappa_0(u(0) - g_0) \quad (2.17b)$$

$$au_x(l) = \kappa_1(u(l) - g_l) \quad (2.17c)$$

In the heat transfer case $a = \lambda$, $u = T$. A Robin boundary condition is applied where in the heat transfer case κ is the heat transfer coefficient and g is the ambient temperature.

$$\begin{aligned} \int_0^l f \nu dx &= -\int_0^l (au_x)_x \nu dx \\ &= \int_0^l au_x \nu_x dx - a(l)u_x(l)\nu(l) + a(0)u_x(0)\nu(0) \\ &= \int_0^l au_x \nu_x dx + \kappa_l(u(l) - g_l)\nu(l) + \kappa_0(u(0) - g_0)\nu(0) \end{aligned} \quad (2.18)$$

By collecting all u 's on the left hand side, this can be rewritten as

$$\begin{aligned} \int_0^l a u_x \nu_x dx + \kappa_l u(l) \nu(l) + \kappa_0 u(0) \nu(0) = \\ \int_0^l f \nu dx + \kappa_l g_l \nu(l) + \kappa_0 g_0 \nu(0), \forall \nu \in V \end{aligned} \quad (2.19)$$

where $V = \{\nu : \|\nu_x\| < \infty, \|\nu\| < \infty\}$. Change V to the space for all continuous piecewise linear functions V_h and note that the test function ν_i can be switched to the hat functions $\phi_i, i = 1, 2, \dots, N$ spanning V_h .

$$\begin{aligned} \int_0^l a U_x \phi_x dx + \kappa_l U(l) \phi(l) + \kappa_0 U(0) \phi(0) = \\ \int_0^l f \phi dx + \kappa_l g_l \phi(l) + \kappa_0 g_0 \phi(0), \forall \phi \in V_h \end{aligned} \quad (2.20)$$

Inserting the ansatz

$$U = \sum_{j=0}^N \xi_j \phi_j \quad (2.21)$$

in equation 2.20 yeilds an equation of the form

$$(A + R)\xi = b + g \quad (2.22)$$

where $A + R$ is called the stiffness matrix and $b + g$ the load vector. The different matrix and vector entries are given by

$$a_{ij} = \int_0^l a \phi_{j,x} \phi_{i,x} dx \quad (2.23)$$

$$r_{ij} = \kappa_l \phi_j(l) \phi_i(l) + \kappa_0 \phi_j(0) \phi_i(0) \quad (2.24)$$

$$b_i = \int_0^l f \phi_i dx \quad (2.25)$$

$$g_i = \kappa_l g_l \phi_i(l) + \kappa_0 g_0 \phi_i(0) \quad (2.26)$$

2.4.3 Solution procedure

The first step of the numerical solution is to assembly of the Stiffness Matrix and the Load Vector. The procedure, which easily can be automated, is described below according to the solution given by [7]. When the matrices are assembled the solution of equation 2.22 is straight forward.

$$\begin{aligned}
 b_i &= \int_I f \phi_i dx \\
 &= \int_{x_{i+1}}^{x_{i+1}} f \phi_i dx \\
 &= \int_{x_{i+1}}^{x_i} f \phi_i dx + \int_{x_i}^{x_{i+1}} f \phi_i dx \\
 &\approx (f(x_{i-1})\phi(x_{i-1}) + f(x_i)\phi(x_i))h_i/2 \\
 &\quad + (f(x_i)\phi(x_i) + f(x_{i+1})\phi(x_{i+1}))h_{i+1}/2 \\
 &= (0 + f(x_i))h_i/2 + (f(x_i) + 0)h_{i+1}/2 \\
 &= f(x_i)(h_i + h_{i+1})/2
 \end{aligned} \tag{2.31}$$

$$b + g = \begin{bmatrix} f(x_0)h_1/2 \\ f(x_1)(h_1 + h_2)/2 \\ f(x_2)(h_2 + h_3)/2 \\ \vdots \\ f(x_{N-1})(h_{N-1} + h_N)/2 \\ f(x_N)h_N/2 \end{bmatrix} + \begin{bmatrix} \kappa_0 g_0 \\ \vdots \\ \kappa_1 g_1 \end{bmatrix} \tag{2.32}$$

And now equation 2.22 can be solved through a matrix inversion to obtain the finite element solution of the problem.

2.5 Coupling procedure

2.5.1 One dimensional correlation

To create one dimensional heat transfer coefficient (HTC) fields, the following correlation given by [6] is used.

$$Nu_x = 0.0288Re_x^{4/5}Pr^{0.3} \quad (2.33)$$

This correlation is developed for flat plates at conditions where $Re > 5 \cdot 10^5$ and $Pr > 0.5$. By introducing correction factors adjusted to give a solution matching the results of a CFD simulation of non flat surfaces, the correlation is now assumed to valid for the new geometry as the original correlation was for flat plates. In this way can the correlation be used to predict HTCs on the non flat surfaces also for other conditions than the ones it was fitted to.

2.5.2 BCgen2

An inhouse code to create transient air temperature and HTCs for an entire flight mission based on a set of boundary conditions. The output from BCgen2 is used as input to structural calculations. In this project BCgen2 is used for single steady state points as well as for a transient working point change.

2.5.3 BCgen_2D_mapping

This program maps 3D fields exported from CFD softwares onto 2D surface. The 2D field is saved in a file format which can be directly loaded into ANSYS APDL as boundary condition for structural calculations. The resolution of the 2D field is possible to adapt according to the requirements and also a time dimension can be included but this function will not be evaluated in this report.

2.5.4 Conjugated CFD

Conjugated CFD differs from ordinary CFD in that it resolves the heat transfer also in specified structural parts such as walls. By solving both the fluid dynamics and the structural temperature in the same simulation a two way coupling is achieved. Typically, conjugated CFD is too computationally demanding to be applied in routine calculations for large structures. This especially becomes a problem in transient simulations where the simulations often will required timescales in weeks. [16]

2.6 Frössling correlation

The Frössling correlation is based on the work of Nils Frössling on boundary-layer flow for two-dimensional and rotationally symmetrical bodies [5]. The results are modified to take turbulence into account and measurements for cylinders in cross flows are used to fit the correlation to the measured results. The correlation can be

2. Theory

applied on the leading edge which can be approximated with a cylinder segment. This allows HTC's to be predicted without the need for simulations.

3

Methods

3.1 2D boundary layer

The first case was a 2D representation of a boundary layer. For simplicity, all walls except the part of the lower boundary of interest, were defined as symmetries, see figure 3.1. Three different methods were compared to test the validity of different assumptions. The first method was to create boundary conditions using a correlation while the second one was to use CFD simulations and export the resulting fields of relevance. In both these cases the inhouse code BCgen2 were used to rewrite the 1D fields into boundary condition files. As a reference case a conjugated CFD simulation was conducted.

The correlation, shown in equations 2.33, is a flat plate correlation relating the Nusselt number to the local Reynold number and the Prantdl number. Fluid properties were taken at the inlet bulk temperature as well as at an adiabatic wall temperature calculated through an adiabatic CFD simulation. The second method included a CFD simulation using a constant wall temperature. The resulting heat flux was extracted from the result file and used to calculate the effective heat transfer coefficient, HTC, at each point of the wall with the same reference temperatures used in case one.

$$HTC = \frac{Wall\ Heat\ Flux}{T_{wall} - T_{ref}} \quad (3.1)$$

A sensitivity analysis for the assumed wall temperature was performed to make sure that the result was not dependent on this estimation. BCgen2 was then used to rewrite these 1D fields of adjacent wall temperatures and HTCs from method two into working boundary condition files. A structural mesh was produced using Hypermesh and the final structural simulations were done in ANSYS Mechanical.

Finally in the conjugated case the wall thickness was resolved within ANSYS Fluent and the boundary conditions on the opposite side of the wall, the cooling side, were set to constant HTC and temperature as done in the FE analysis (FEA). Exporting the wall heat flux and using equation 3.1 as with the constant wall temperature CFD, resulted in a third HTC which could be compared to the others as a reference case. Concluding this steady part of the 2D boundary layer, a comparison of the resulting wall temperatures was done.

3.1.1 Mesh and settings

To find a good CFD mesh of reasonable size an initial mesh study was conducted. Four meshes were constructed in ANSYS® Meshing. The four meshes differed in

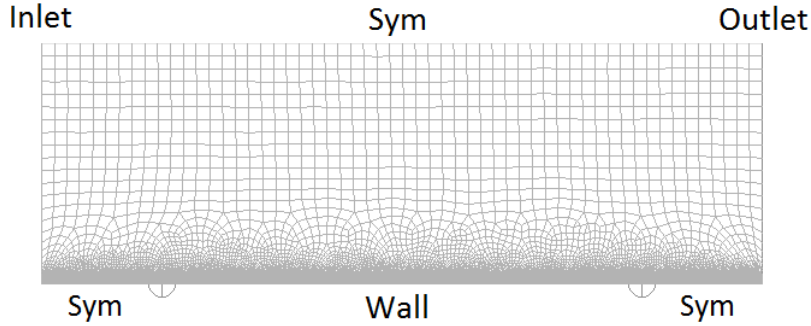


Figure 3.1: Mesh used in the 2D-Duct case. The points marks the edges of the wall.

their wall and bulk resolutions and were all in the interval of 26,800 to 73,000 elements. The goal was to identify the coarsest mesh possible resulting in an easily converged solution with y^+ values below 1 on the main part of the wall. It should also have a maximum aspect ratio values close to 100 or below. Simulation were done for all meshes and the resulting wall heat fluxes were plotted in the same plot to reveal potential differences.

| | Body cell size [m] | First inflation layer thickness [m] | Wall sizing [m] | No. of cells |
|--------|--------------------|-------------------------------------|-----------------|--------------|
| Mesh 1 | 7e-3 | 3e-6 | 3e-4 | 73000 |
| Mesh 2 | 7e-3 | 7e-6 | 7e-4 | 27600 |
| Mesh 3 | 1e-2 | 7e-6 | 5e-4 | 37900 |
| Mesh 4 | 1e-2 | 9e-6 | 7e-4 | 26800 |

Table 3.1: The different meshes tested

The mesh is shown in figure 3.1 and the body cell size in table 3.1 can be seen as the cell size in the main body of the mesh, i.e. the largest cells in the figure. The first inflation layer thickness is the thickness of the cells closest to the wall measured from the wall while the wall sizing is the length of the cells closes to the wall in direction along the wall. The number of cells gives the total number of cells in the mesh.

Once the best mesh was chosen sensitivity analyses of the inlet boundary conditions and the wall temperature was carried out. Reasonable boundary conditions, Case A, were constructed based on recommendations by [4] and knowledge about upstream structures. This case was chosen as mid value in the sensitivity analysis and the turbulent length scale was set to 10 % of the channel height. To test the dependence of the solution on these values a set of alternative boundary conditions were constructed listed in the table below.

The resulting wall heat fluxes were compared to see in which extent the results depend on the boundary conditions. In the wall temperature analysis temperatures between 400 and 800 K were tested.

For the simulations the realizable $k-\epsilon$ model was used and at the wall of constant

| | Turbulent Intensity [%] | Turbulent Length Scale [m] |
|--------|-------------------------|----------------------------|
| Case A | 5 | 0.0095 |
| Case B | 10 | 0.0095 |
| Case C | 2 | 0.0095 |
| Case D | 5 | 0.085 |
| Case E | 5 | 0.002 |

Table 3.2: Inlet parameter setups tested

temperature 600 K, enhanced wall treatment was enabled including models for pressure gradient effects, thermal effects and viscous heating. A no slip condition was also specified. A mass flow inlet was used together with a pressure outlet.

To perform the conjugated simulations a thermal convection boundary condition was applied to the wall section. The wall was defined to be 2 mm thick and the thermal conduction was governed by the outer wall flow properties set to 700 K with a HTC of $40\text{ W}/(\text{m}^2\text{ K})$. Material properties was estimated with values found for Inconel 625 at [3]. For thin walls, as in this case, only constant conductivity was possible thus the conductivity was specified to be $14.2\text{ W}/(\text{m K})$. Another limitation of ANSYS Fluent was that only 1D conduction was possible for 2D simulations.

3.2 Hub film

In this case the effect of a leak flow, entering the exhaust gas path in a turbine rear structure, on the hub surface temperature profile was examined. As part of this also the vane surfaces were included in this analysis. Cold air, drained from the compressors, is typically used to cool the inner surfaces of the structure by injection into the disc cavity. This air will enter the exhaust gas path through the spacing between the last rotor row in the low pressure turbine and the static turbine rear structure where it will create a film on the hub surface. Two different geometries were used; one modified version of the cascade facility existing at Chalmers University of Technology and an existing structure at GKN Aerospace.

As in the previous case initial CFD simulations were made. The expectation was to find a horseshoe vortex that enhances the mixing around the vane and pulls down hot gas to the hub surface. [10] The mixing factor, η , was introduced to describe the level of mixing. By assuming that the mixing behaviour is constant for all flow conditions, the same mixing coefficient field can be used in several different flow conditions without the need of performing demanding CFD simulations for each case. The adiabatic CFD simulations used to calculate η is defined with no heat transfer between any of the walls and the adjacent fluid. This means that the local fluid temperature at the wall is a function of the amount of mixing and the two inlet temperatures. η , is defined as $T_w = \eta T_1 + (1 - \eta) T_2$ where T_w is the fluid temperature at the wall, T_1 is the total leak flow temperature and T_2 is the total gaspath inlet temperature. When the mixing factor is known the local bulk temperature can be calculated from the inlet temperatures. Since a CFD exists for this case the use of η will yield the same results as using a temperature field directly.

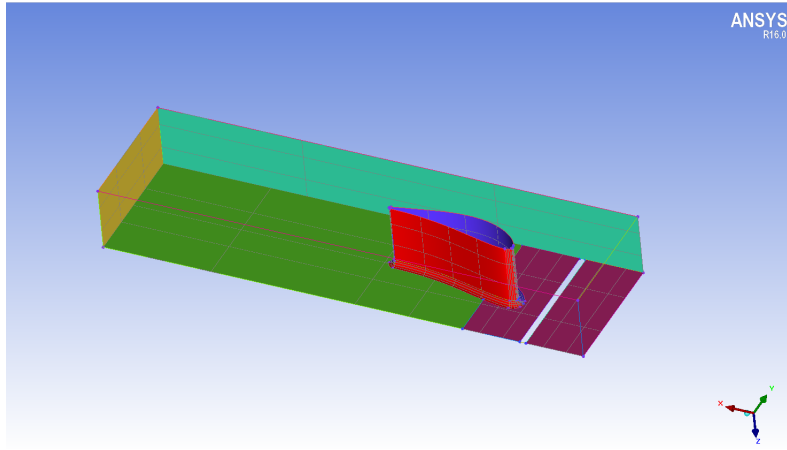


Figure 3.2: The cascade geometry used in the simulations.

HTC was calculated as in the 2D boundary layer case with a constant wall temperature CFD simulation. The resulting fields of η and HTC were then transformed into boundary condition files using the inhouse codes BCgen2 for 1D fields and BCgen_2D_mapping for 2D fields. 1D fields were easily produced directly in ANSYS Fluent using the function "circumferential-averaging-axial", but the exported fields has to be modified by BCgen2 before implementation as boundary conditions. For the loads on the cascade geometry, different combinations of 1D and 2D fields of η and HTC were tested to find the most influential parameter and the most critical parts to resolve. Lessons from this first test was then utilised while evaluating the existing geometry both in terms of temperature profiles and resulting material stresses which affects the components structural life.

3.2.1 Mesh test and sensitivity analysis

All meshes were structured and they were created using ANSYS ICEM 16.0. The existing cascade geometry was modified with a strut fillet radius and by the creation of a leak flow inlet slot. An appropriate mesh fulfilling the best practice guidelines at GKN Aerospace was initially created consisting of 1,960,000 cells, Mesh A. From this mesh further refinements of the domain were made and resulted in two finer meshes, B and C, with 3,170,000 and 6,620,000 cells respectively. A mesh study was conducted which compared the mixing factor in 200 tangentially averaged bands on the hub surface as well as 50 bands on the pressure and suction side of the vane where the bands were averaged in the radial direction. Further, a sensitivity analysis of the the inlet temperature's effect on the heat transfer coefficient as well as it's effect on the mixing factor, η , was performed on mesh 1. The HTC is calculated using equation 3.1 on results achieved from a CFD simulation assuming constant wall temperature and that both inlets have the bulk inlet temperature. The later assumption is made to avoid problems with the sign of the HTC. It is important that its value is not sensitive to changes in either inlet temperature or wall temperature and therefore both these temperatures were subjected to sensitivity analyses.

3.2.2 Testing of the method

To verify that the current procedure is accurate enough, simulations according to present best practise guidelines were made. As comparison and to identify alternative procedures different thermal loads were tested where the dimension of the η and HTC fields were varied. As reference case a conjugated CFD analysis was used. Conjugated CFD is two way coupled and utilises a finer wall mesh than the FEA and should therefore yield a result closer to the reality.

In the simplest case a zero dimensional field can be used. This is a very coarse estimation in many cases and to include some variations a 1D fields varying in the x -direction can be applied which carries slightly more information. A 2D field should be able to resolve also the effect of the horseshoe vortex surrounding the blade which are expected to be significant and also other effects varying in the tangential direction. Currently a 1D approach is conducted and to test whether or not the assumption that this approximation is reasonable, eight different thermal loads were created:

1. 1D load on blade and hub
2. 1D load on blade, 1D η and 2D HTC on hub
3. 1D load on blade, 2D η and 1D HTC on hub
4. 1D load on blade, 2D on hub
5. 2D load on blade, 1D on hub
6. 2D load on blade, 1D η and 2D HTC on hub
7. 2D load on blade, 2D η and 1D HTC on hub
8. 2D load on blade and hub

Since the temperature difference over the blade was neglectable, a zero dimensional temperature field was applied on both the pressure side and suction side throughout all calculations while the HTC field was varied.

4

Results

4.1 2D boundary layer

This section presents the results of the initial tests to find a suitable mesh and the following sensitivity tests. This is done for the inlet boundary condition and the wall temperature as well as results from the final simulations.

4.1.1 Mesh test

The mesh test did not show any significant differences in the results of the different simulations. For the meshes with less wall resolution a small difference in the wall flux at the first 5 mm of the plate could be spotted but this was assumed negligible and a coarse mesh could be used. Mesh D was therefore chosen for future simulations. The mesh quality of Mesh D is presented in table 4.1 below. The meshes were compared in terms of the resulting heat flux over the wall and the results are presented in figure 4.1

| | Minimum | Average | Max |
|--------------------|------------|---------|---------|
| Orthogonal quality | 0.49861 | 0.99121 | 1 |
| Skewness | 1.3057e-10 | 0.10004 | 0.79043 |
| Aspect ratio | 1 | 10.665 | 78.871 |

Table 4.1: Quality of Mesh D

The recommended values for orthogonal quality according to the Fluent User's guide [12] are a minimum orthogonal quality above 0.1 with a significantly higher mean value. It also mentions that extreme aspect ratios can be acceptable in regions without strong gradients or large changes. [1] gives a recommendation to keep the aspect ratio below five in general and possibly higher along the walls. The maximum skewness should be below 0.95 and the average below 0.33. The values in table 4.1 fulfills the requirements which results in a good convergence of the simulations. The high aspect ratio cells are all aligned with the wall and the high values depend on the low first layer height used to resolve the boundary layer and achieve a y^+ value below one.

4.1.2 Inlet boundary conditions

The sensitivity analysis of the inlet boundary conditions showed that the specified turbulence parameters had some influence on the results on the entire domain which

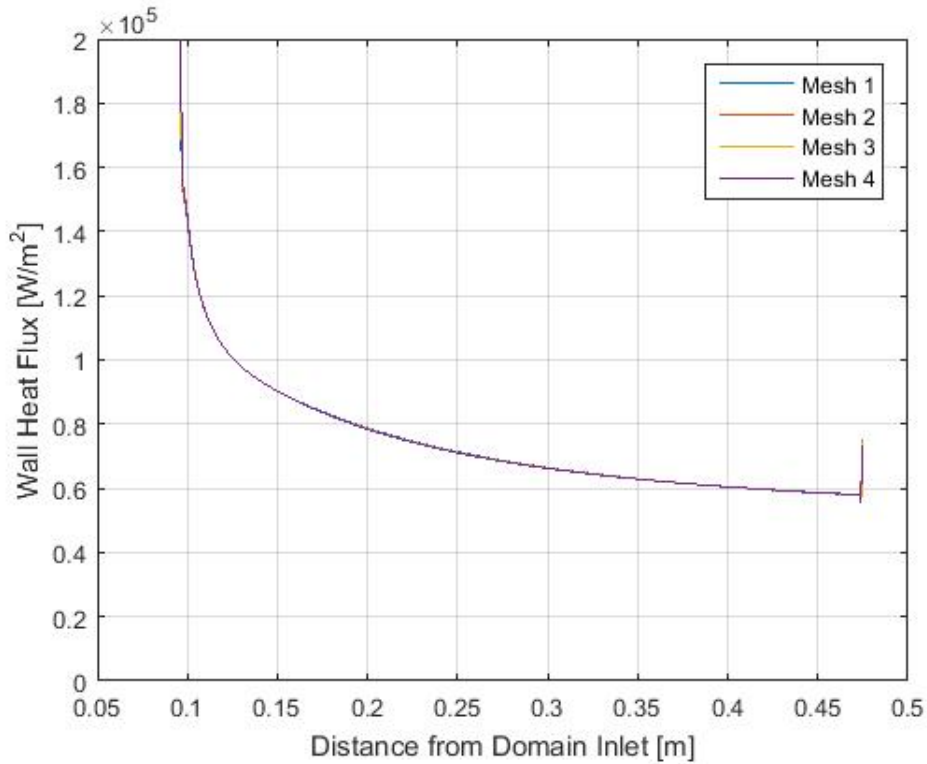


Figure 4.1: Mesh sensitivity analysis. Comparison of wall fluxes using meshes A-D.

is expected since the level of turbulence affects the convective heat transfer. As seen in figure 4.2 the difference in the results was small and therefore the baseline inlet boundary conditions, Case A, was deemed good.

4.1.3 Wall temperature dependence

From fig 4.3 it can be seen that the choice of wall temperature clearly has an effect on the resulting HTC value. The air inlet temperature was set to 840 K in all cases, and it can be seen that the HTC goes down steeply when the wall temperature gets closer to this value. This means that it is important to choose a T_w close to the real value when the HTC is calculated. Equation 3.1 can be regarded as a linearisation of the heat flux around the chosen T_w .

if, in the determination of HTC, ΔT is high, HTC will be high and this will result in a smaller steady state ΔT since a temperature difference between metal and gas will result in a higher heat flux. The opposite will be the case with a lower ΔT evaluating HTC.

4.1.4 Steady state simulations

The comparison between achieved thermal profiles of the wall using correlation, one way coupled CFD-FE and conjugated analysis is showing an overestimation of the metal surface temperature of approximately 5 K compared to the conjugated anal-

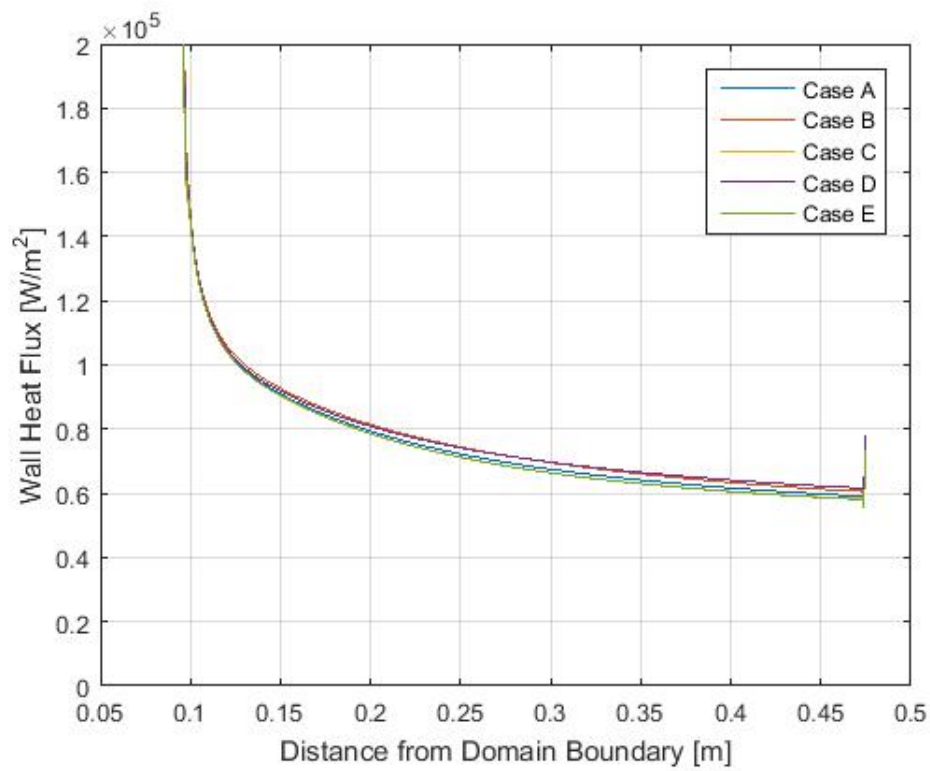


Figure 4.2: Comparison between different inlet conditions specified in table 3.2.

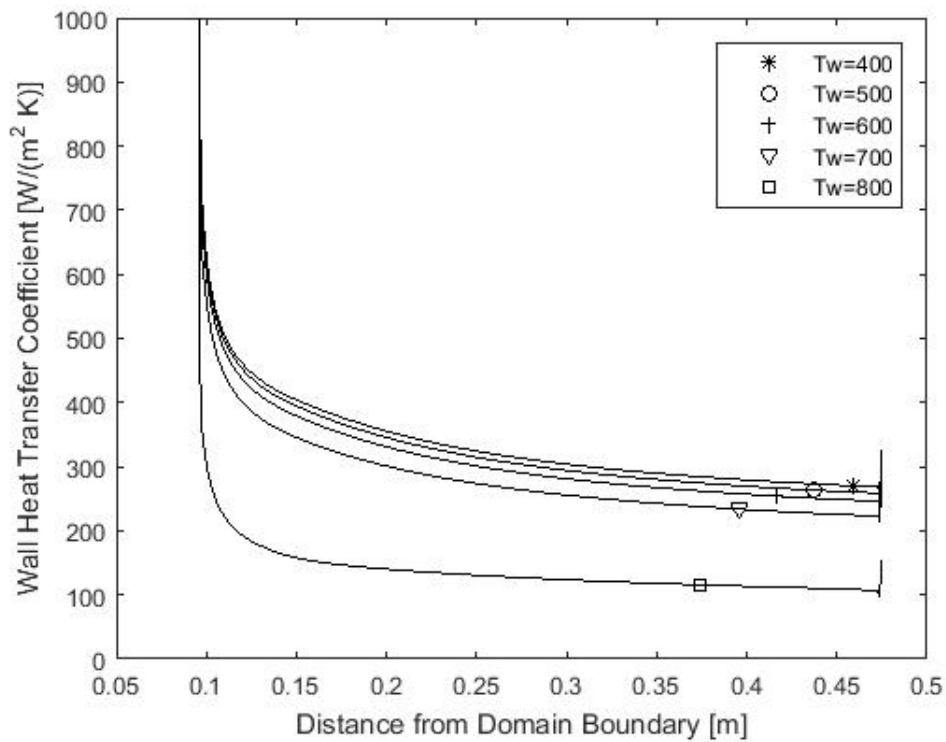


Figure 4.3: Comparison of resulting HTC's using different fixed wall temperatures.

ysis using the total air inlet temperature as reference temperature. Instead taking the reference temperature as the area weighted average of the near-wall-temperature from an adiabatic simulation resulted in good agreement with the conjugated CFD.

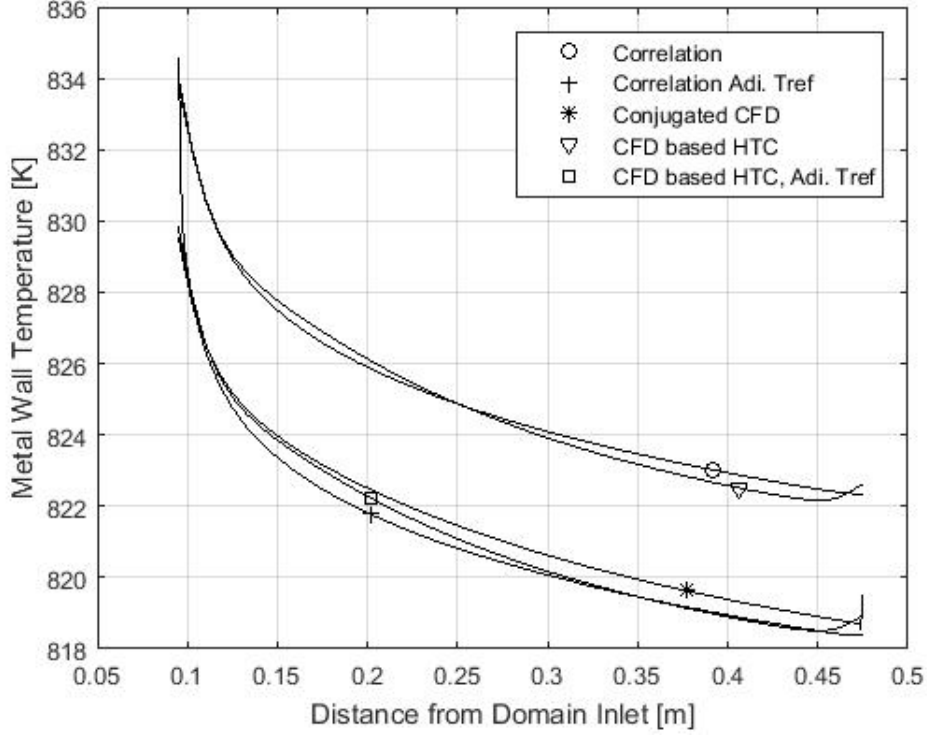


Figure 4.4: Metal wall temperatures resulting from different methods. In the adiabatic cases has an adiabatic cfd simulation been performed to calculate the fluid temperature at the wall temperature. An area weighted average of 816.34 K was used as reference temperature in these cases. Otherwise the inlet bulk temperature of 840 K was used

The resulting difference in metal temperature could easily be shown to be closely correlated to the difference in reference temperature by making a simple heat balance over the wall using the same specified parameters. At steady-state the heat fluxes must be balanced on both sides of the wall, $Q_1 = Q_2$. This can also be written as

$$HTC_1(T_{1,ref} - T_{2,w}) = -HTC_2(T_{2,ref} - T_{2,w}) \quad (4.1)$$

Neglecting the temperature profile through the wall ($T_{1,w} = T_{2,w} = T_w$), this can be simplified to

$$HTC_1(T_{1,ref} - T_w) = -HTC_2(T_{2,ref} - T_w) \quad (4.2)$$

which can be written as

$$T_w = \frac{HTC_1 T_{1,ref} + HTC_2 T_{2,ref}}{HTC_1 + HTC_2} \quad (4.3)$$

Equation 4.3 is plotted in figure 4.5 as $T_w(T_{ref})$ by making reasonable approximations, assuming the initial flux to be $Q_{1,0} = 80,000 W$, $HTC_2 = 40 W/m^2 K$,

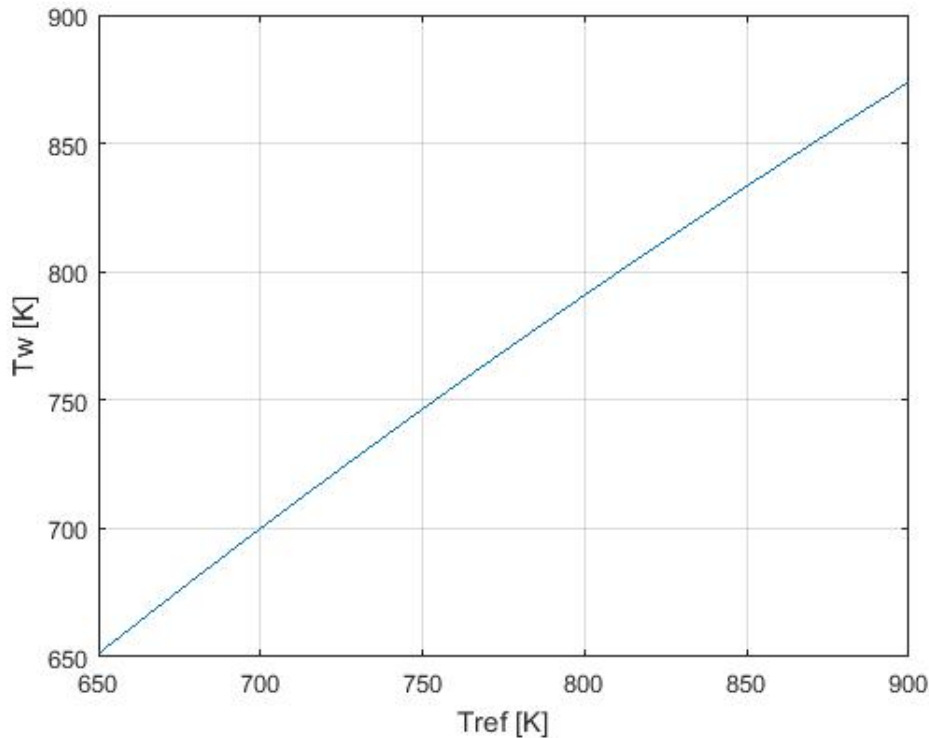


Figure 4.5: Wall temperature as a function of the reference temperature.

$T_{2,ref} = 700 K$ and $T_{1,ref} = 600 K$. HTC_1 can thereby be calculated using equations 3.1.

This simple analysis shows that the resulting wall temperature is clearly dependent on the reference temperature. And the question is thereby, why does the fluid wall temperature deviate from the total bulk temperature?

In his book *Boundary-Layer Theory* [13] Dr. Hermann Schlichting explains this phenomena as a consequence of compressibility effects. For a flat plate with zero incidence the adiabatic wall temperature can be calculated as

$$T_{bulk} = T_{static} + \sqrt{Pr}(T_{total} - T_{static}) \quad (4.4)$$

The Prandtl number for air is approximately equal to 0.71 [8] which simplifies the formula to

$$T_{bulk} = 0.16T_{static} + 0.84T_{total} \quad (4.5)$$

The static temperature is seldom known directly in engine development but can be calculated from the total temperature and the velocity through the following expression:

$$T_{static} = T_{total} - \frac{v}{2C_p} \quad (4.6)$$

where v is the velocity. [11] Fluent gave a static temperature at the inlet of $808.82K$. Insertion into equation 4.5 together with a total temperature of $840K$ gives an estimated adiabatic temperature of $835K$ which can be compared to the area weighted averaged temperature given by the adiabatic fluent analysis, $835.5K$. By using this

adiabatic temperature as reference temperature it is guaranteed that the resulting wall temperature will not reach a value higher than the effective fluid temperature adjacent to the wall. Such unphysical behaviour was observed when using the total bulk temperature as reference temperature without taking the breaking losses into account.

When trying to resolve these breaking losses the near wall effects was found to play an important role in the simulations. Including the effects of viscous heating, thermal effects and pressure gradient effects resulted in a $19.5K$ increase of the adiabatic wall temperature compared to simulations omitting these effects (not included in figure 4.4). The new, higher, value compared much better with existing correlation and is therefore seen as more accurate.

4.2 Hub film

4.2.1 Mesh test

Mesh 1, 2 and 3 were used in adiabatic simulations to calculate the mixing coefficient. The results were averaged over 200 bands on the hub surfaces and 50 bands on each side of the blade to make the field one dimensional. The results are plotted in the x direction in figures 4.6a-4.6c. The results shows excellent agreement between the different meshes and hence the coarsest mesh, mesh A, was chosen for further simulations.

4.2.2 Sensitivity analysis for inlet and wall temperature

A sensitivity analysis on the heat transfer coefficient as a function of inlet temperature and wall temperature was conducted. As can be seen in figures 4.7a-4.7c, the HTC is not sensitive to changes in the inlet temperature. The largest deviations occur when the difference between fluid temperature and wall temperatures get small. The deviations mainly occurs at the pressure side leading edge and mid chord suction side and the largest deviation can be seen to be around 8.8%. Except for this particular deviating value at the leading edge the largest deviations occurs within 5.7%.

A very similar behaviour can be observed in figures 4.6d-4.6f, where the wall temperature is varied. Larger temperature difference between fluid and wall gives higher HTCs until the difference is approximately $150^{\circ}C$. When ΔT instead goes under $50^{\circ}C$ the values starts to deviate more rapidly towards lower HTCs. This behaviour can be recognised from the 2D case. Overall the wall temperature has low effect on the results and can be assumed constant. To see whether the differences depend on changes in the mixing behavior an additional adiabatic simulation was done. The results are presented in figures 4.7d-4.7f and it can be seen that the deviations occurs in the same regions as the HTC-deviations. This means that the heat flux distribution will change with the inlet temperature and this will in turn affect the HTC distribution. The deviations are also found to occur at the positions where the velocity reaches its maximum which could result in mach number effects on the results. These conclusion do not explain the behaviour in the 2D boundary

layer case, where there is no mixing and the surface is flat. The deviations might instead depend on the local bulk temperature differences resulting from changes in the breaking losses of the fluid.

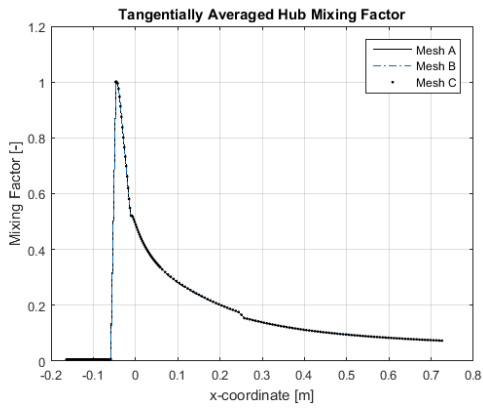
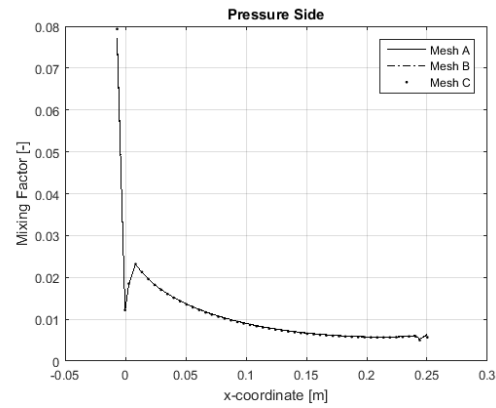
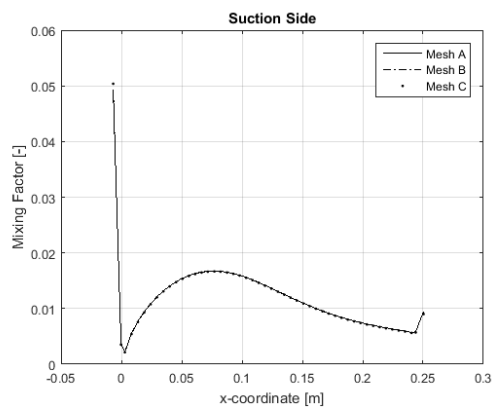
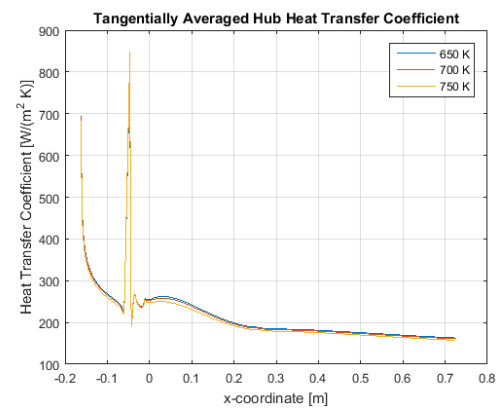
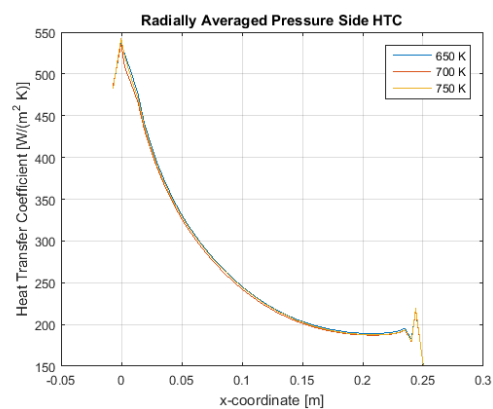
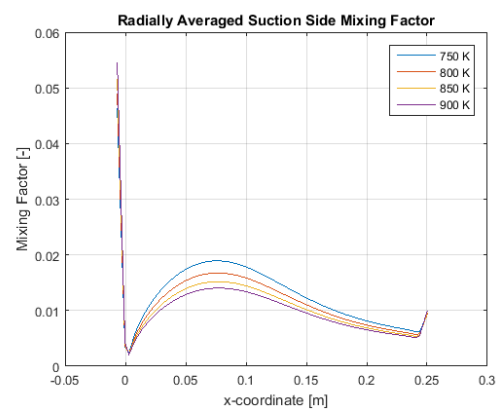
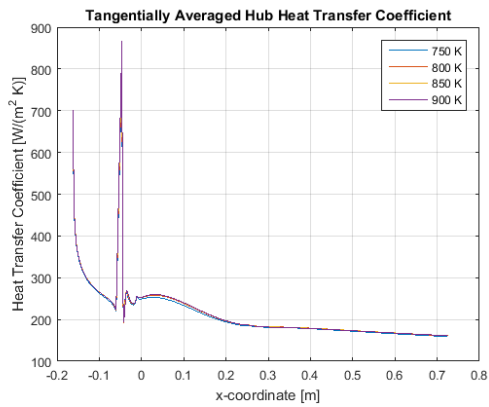
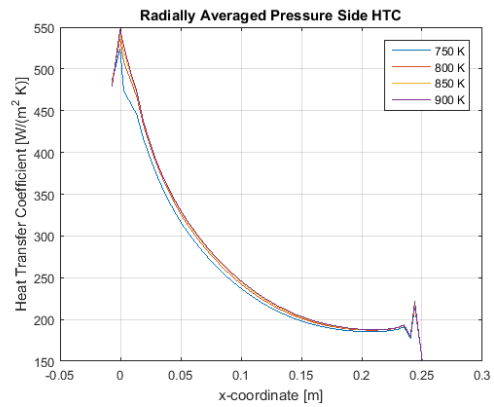
(a) Mesh test hub surface η (b) Mesh test pressure side η (c) Mesh test suction side η (d) T_w , hub surface HTC(e) T_w , pressure side HTC(f) T_w , suction side HTC

Figure 4.6: Meshtest of three different meshes (a-c) and sensitivity analysis for wall temperature (d-f).

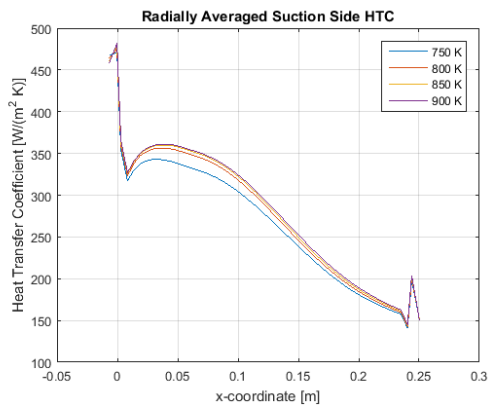
4. Results



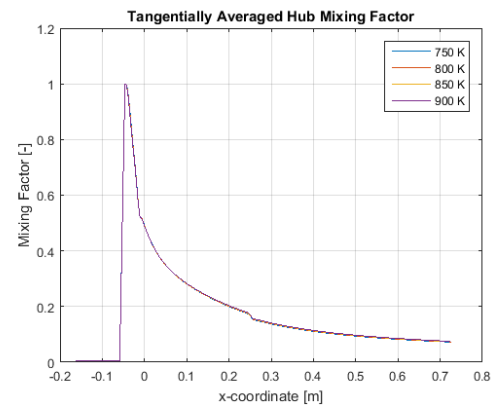
(a) Hub surface HTC



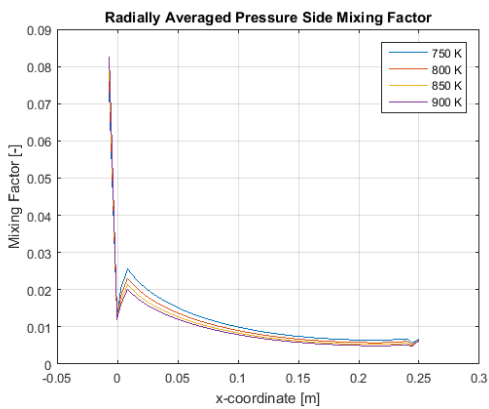
(b) Pressure side HTC



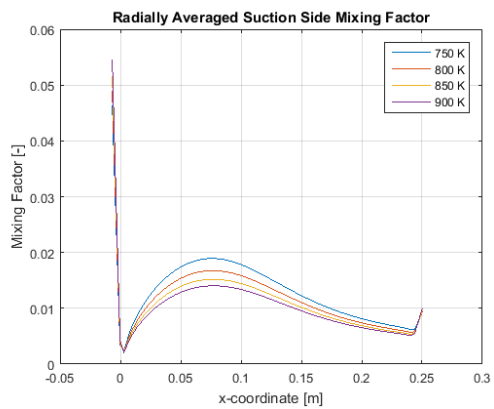
(c) Suction side HTC



(d) Hub surface η



(e) Pressure side η



(f) Suction side η

Figure 4.7: Sensitivity analysis for inlet temperature.

4.2.3 Structural temperature profiles

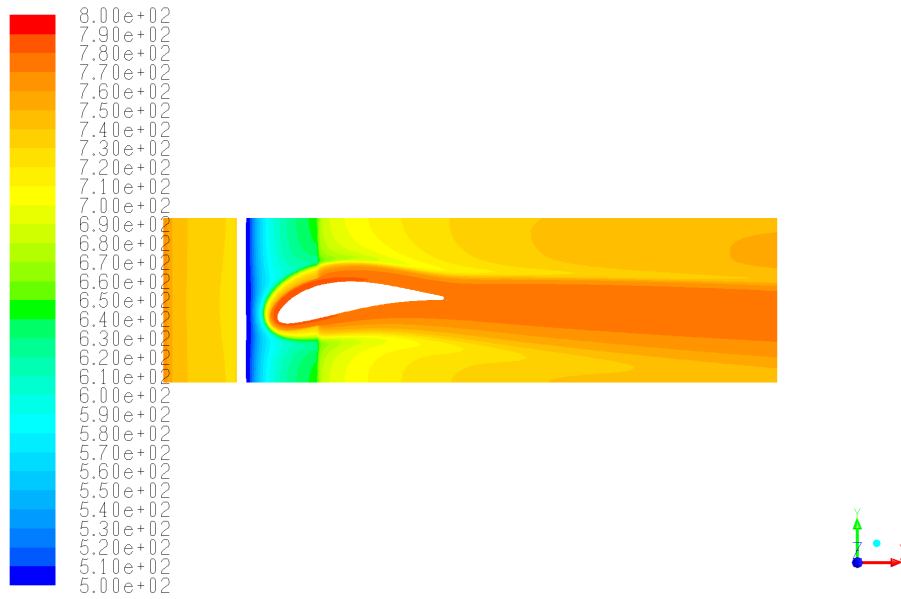
The different cases listed in the Method chapter have been investigated and the resulting thermal profiles are presented in this section.

Figure 4.8 contains contour plots displaying the thermal profiles on the hub surface using 1D fields on the blade. The conjugated analysis and the CFD simulations used to produce the boundary conditions also included the hub surface prior to the leak flow inlet. This was later seen to have an effect on the produced 2D thermal loads from the later cases.

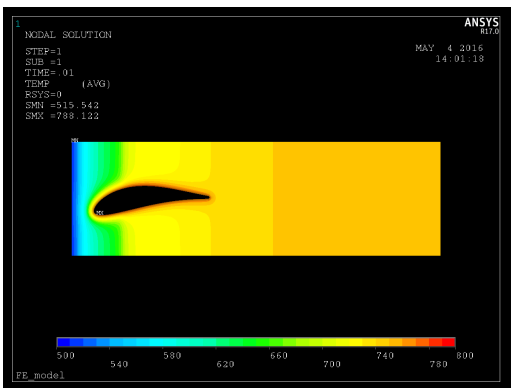
Figure 4.8a shows the conjugated solution on the hub surface. It shows a cold region closest to the leakflow inlet slot. The temperature increases as the cold film produced by the leakflow mixes with the hot bulk flow. The effects of the horseshoe vortex is seen as a hot region surrounding the blade where it enhances the mixing and pulls down hot air to the surface. Partly, this high temperature also depend on conduction from the blade which is fully exposed to the higher gaspath temperature. The horseshoe vortex also causes the hot wake region trailing the blade. At around 30 % of the blade chord length a sharp temperature increase is seen. This phenomena is present due to a wall on the underlying surface which splits the underlying space into two separate cavities. The first one, causing the leakflow, is the coldest one while the rear cavity, also including the blade interior, is slightly hotter. This temperature difference causes higher cooling effect on the leading part of the hub surface.

Looking at the contours from the FEA it can be seen that 1D fields are not enough to resolve either the hot area surrounding the blade or the hot wake. A slight difference can be seen when applying a 2D field of HTC but the difference is very small. Instead applying a 2D field for the mixing coefficient, η , a clear temperature at both the blade fillet radius and in the wake area resembling the one from the conjugated simulation. Applying 2D fields for both coefficients improves the results further but it is obvious that the mixing coefficient is the most important parameter. It should be noted that when applying a 2D field for the mixing coefficient the results fails to resolve the cold area closest to the leakflow inlet slot. Figure 4.9 Shows the same results as figure 4.8 but with 2D HTC fields on the blade instead of 1D. As can be seen this did not have any effect on the hub temperature profile.

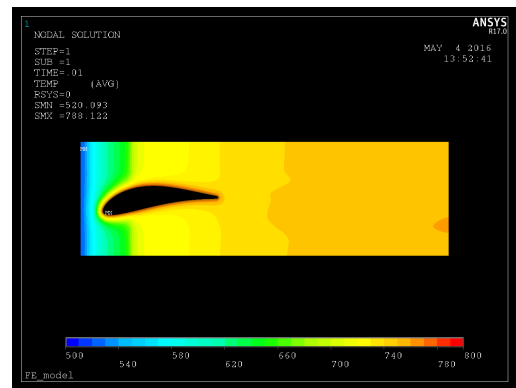
4. Results



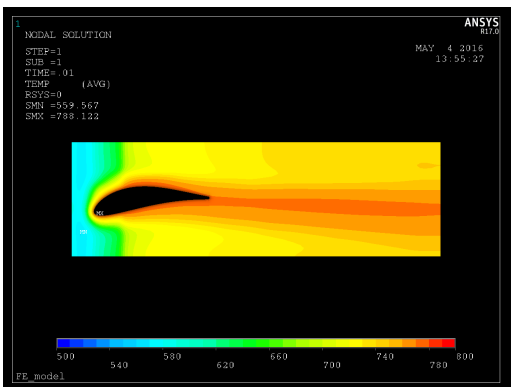
(a) Conjugated Analysis



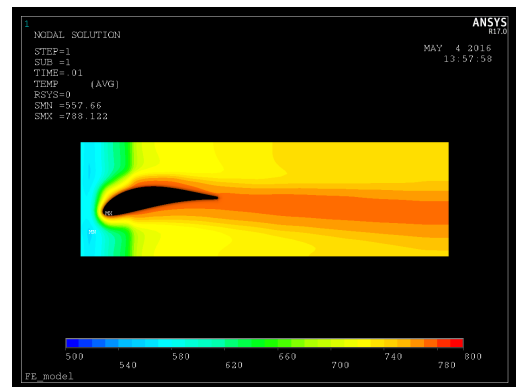
(b) 1D fields



(c) 1D η and 2D htc

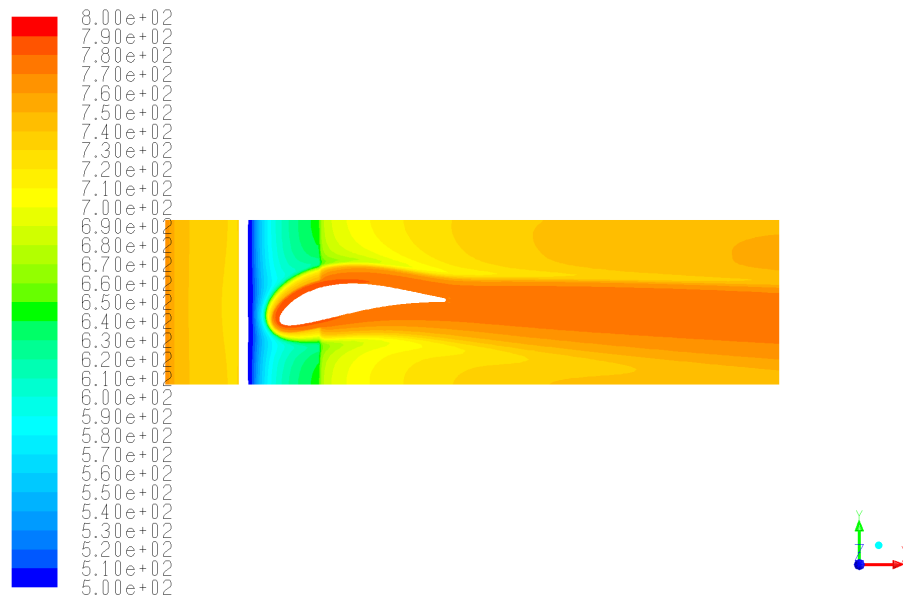


(d) 2D η and 1D htc

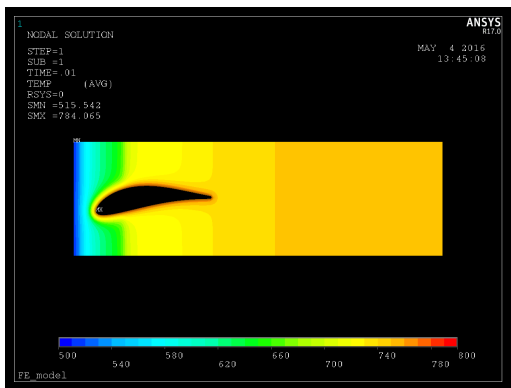


(e) 2D fields

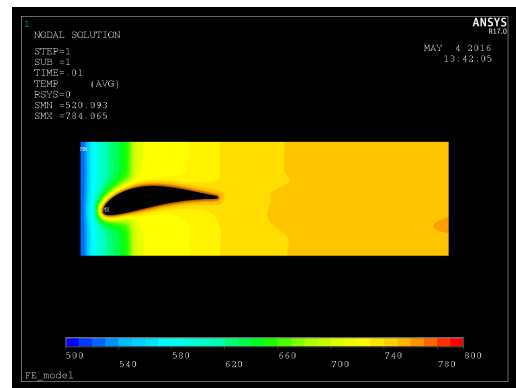
Figure 4.8: Resulting wall temperatures using 1D blade fields with varying hub fields



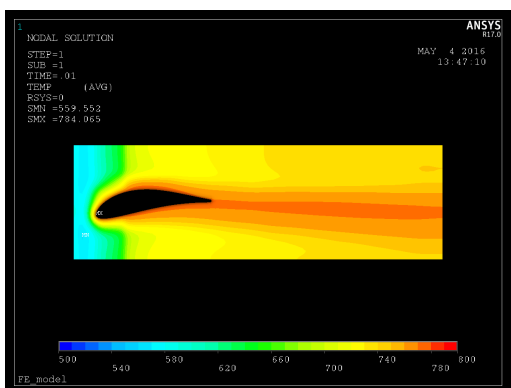
(a) Conjugated Analysis



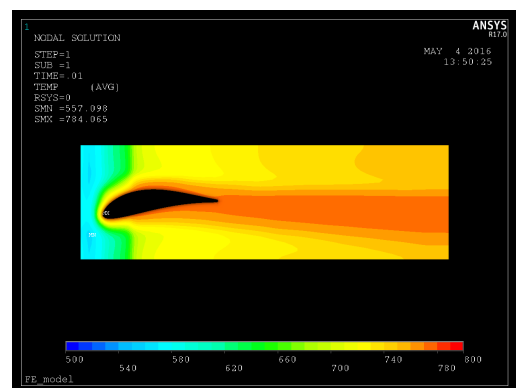
(b) 1D fields



(c) 1D η and 2D htc



(d) 2D η and 1D htc

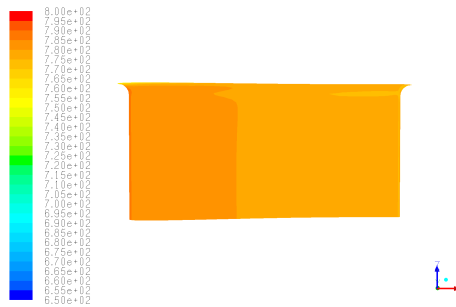


(e) 2D fields

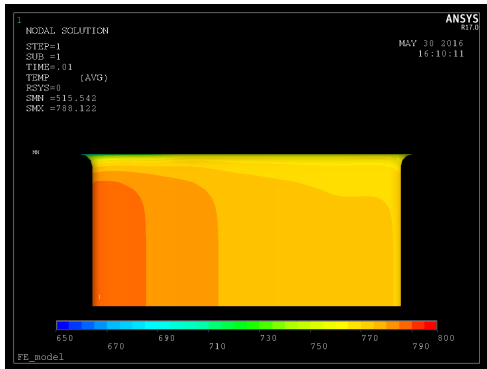
Figure 4.9: Resulting wall temperatures using 2D blade fields with varying hub fields

4. Results

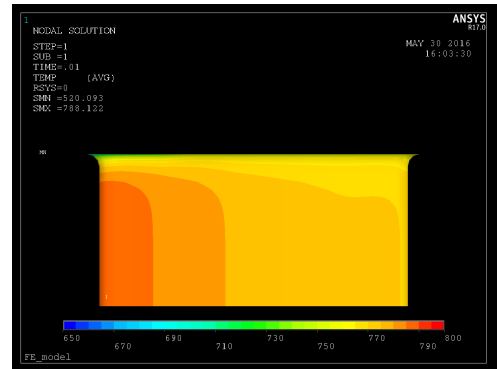
Moving on to figure 4.10 and 4.11 which displays the thermal profile on the vane. The conjugated simulations shows a hot region at the leading edge and also the effects of the horseshoe vortex can be seen at the fillet radius at both the pressures side and the suction side. The contours from the FEA shows that it is hard to describe these features. All simulations done by the one way coupling underestimates the fillet temperature and fails to resolve the horseshoe vortex effects. It can also be seen that the dimensions of the thermal loads applied the the hub surface do not have any significant effect on the thermal profile on either side of the blade. A slight improvement can be observed at the trailing edge close to the hub surface.



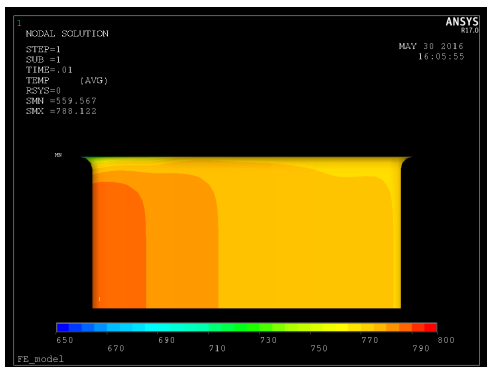
(a) Conjugated Analysis



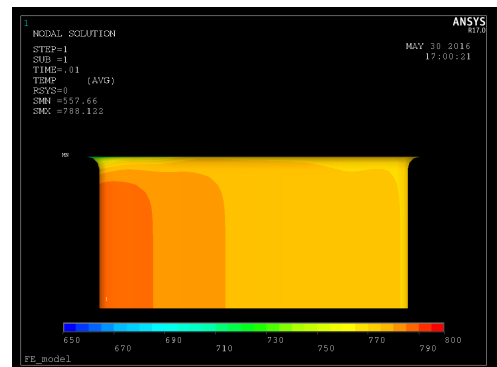
(b) 1D fields



(c) 1D η and 2D htc

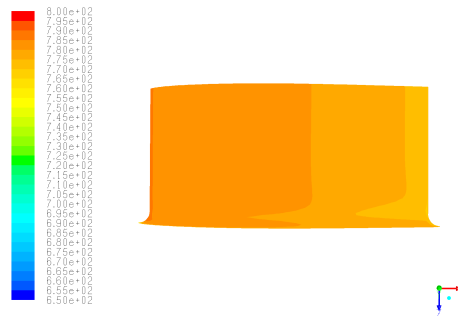


(d) 2D η and 1D htc

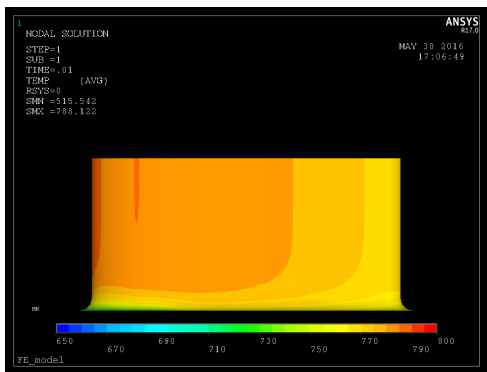


(e) 2D fields

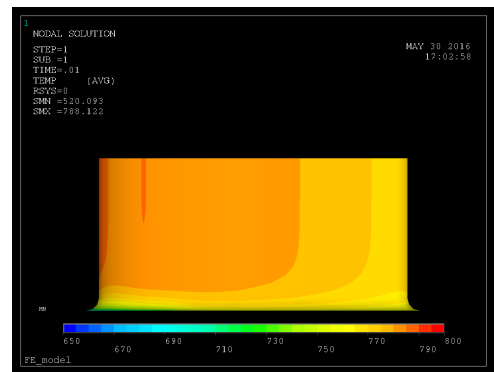
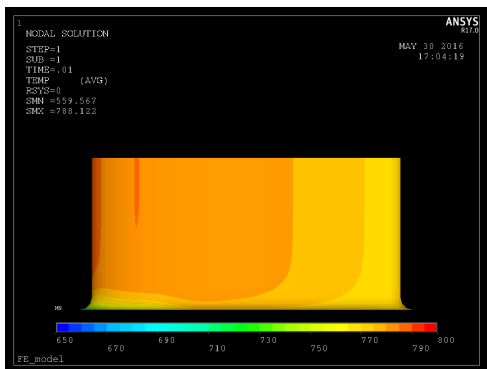
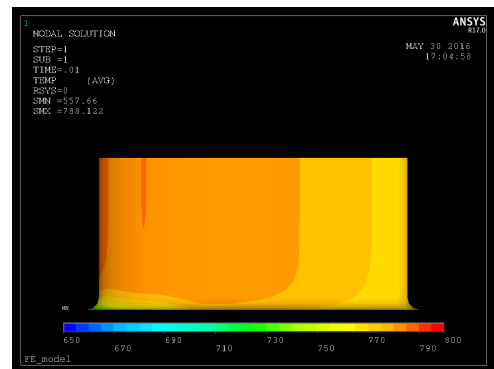
Figure 4.10: Resulting pressure side blade wall temperatures using 1D blade fields with varying hub fields



(a) Conjugated Analysis



(b) 1D fields

(c) 1D η and 2D htc(d) 2D η and 1D htc

(e) 2D fields

Figure 4.11: Resulting suction side blade wall temperatures using 1D blade fields with varying hub fields

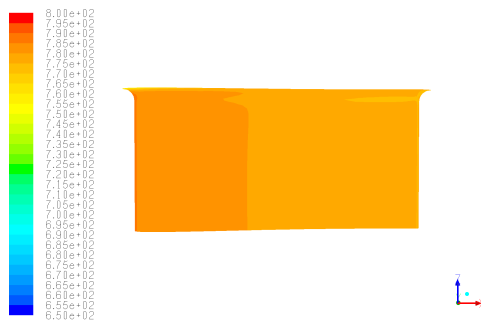
Figure 4.12 shows a comparison between the contours resulting from 1D and 2D fields applied to the blade surfaces. This comparison shows that the 1D fields actually performs better in this case where the 2D fields seems to cause an underestimation of the temperature. In any case, the difference is small.

As mentioned, all simulations underestimates the leading edge fillet temperature. To test whether the resolution of the applied thermal load was responsible for the problems further tests were made. Since the structure is approximately 90cm long it is unlikely that the 20 points used can accurately resolve a structure of 1 cm which is the size of the fillets. To test hypothesis this three finer grids of 40x40, 80x80 and

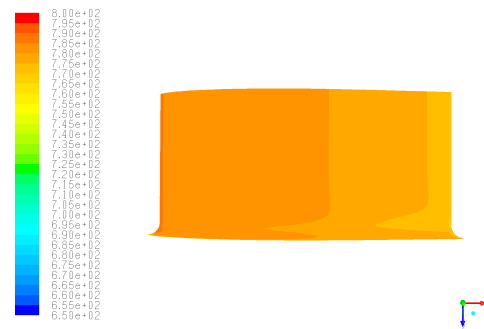
4. Results

200x200 elements respectively, were created which required a minor modification of the software. The applied fields are shown in figure 4.13.

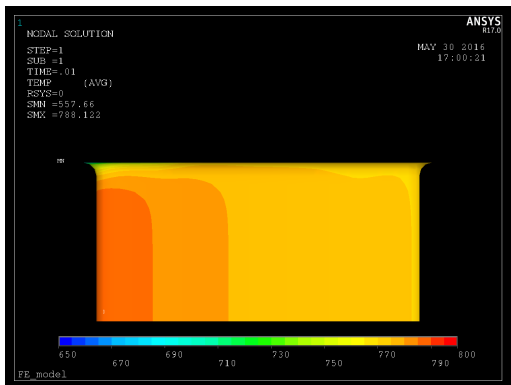
As expected is the 20x20 resolution not sufficient to resolve the hot temperature field surrounding the vane. With 40x40 points the hot area becomes continuous and it gets thicker with further increases of the resolution. By looking at the area closest to the leak flow inlet slot, it can be concluded that the error in the temperature predictions is created in the production of these loads. When using a CFD field con-



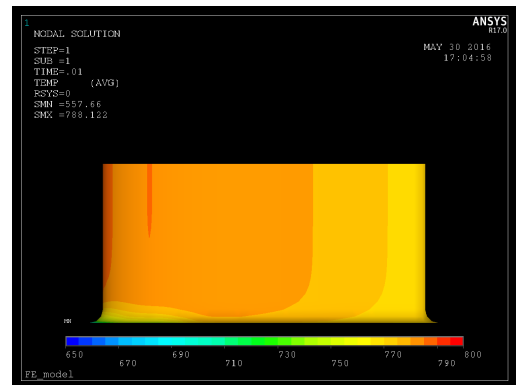
(a) Conjugated analysis - ps



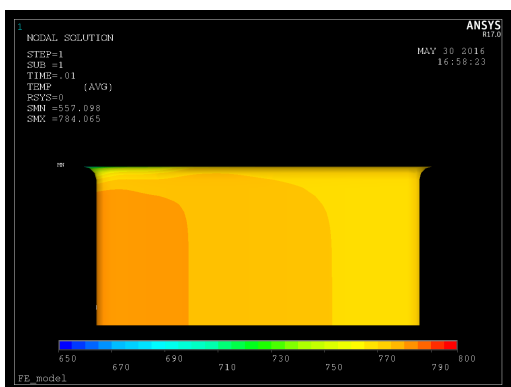
(b) Conjugated analysis - ss



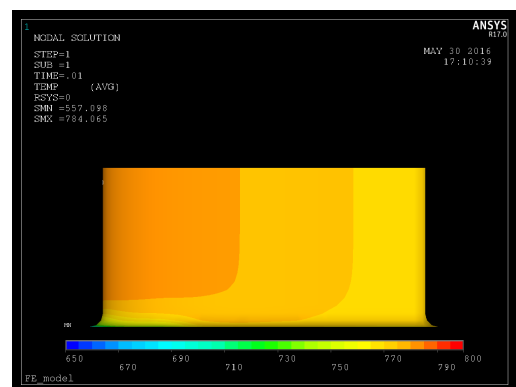
(c) 1D htc blade field - ps



(d) 1D htc blade field - ss

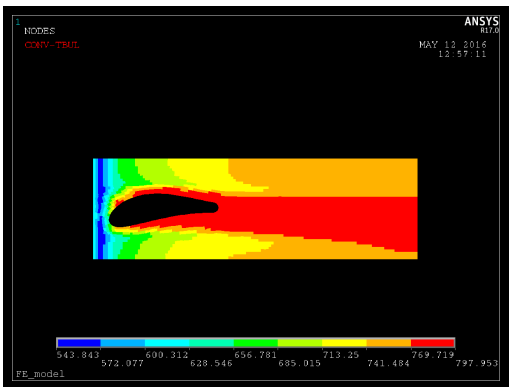


(e) 2D htc blade fields - ps

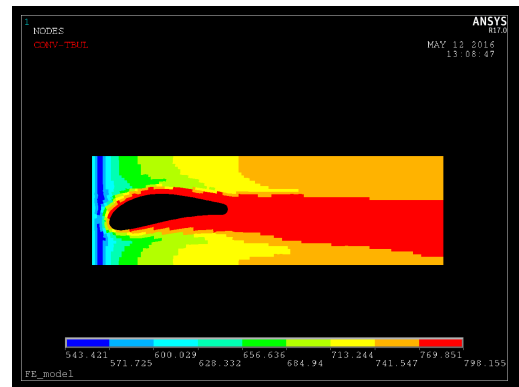


(f) 2D htc blade fields - ss

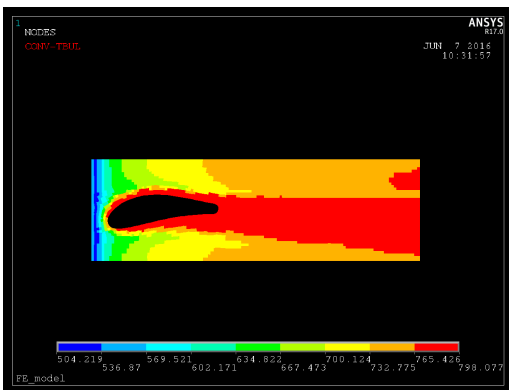
Figure 4.12: Comparison between 1D and 2D htc blade fields' effect on blade surface temperature with 2D hub field



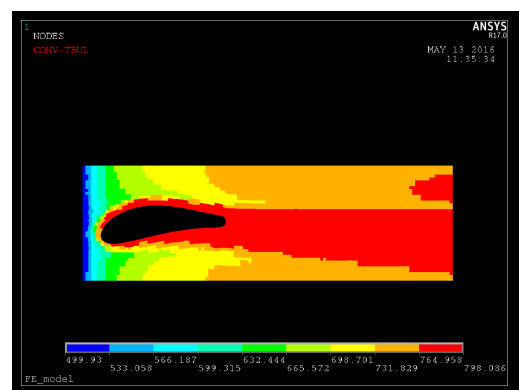
(a) 20x20 elements



(b) 40x40 elements



(c) 80x80 elements



(d) 200x200 elements

Figure 4.13: Applied thermal loads of different resolutions.

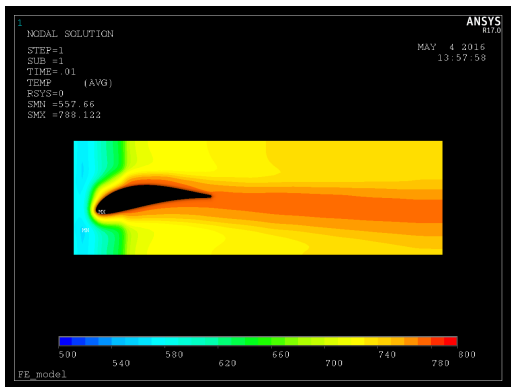
taining the low pressure turbine hub surface situated prior to the leakflow inlet slot, the resulting thermal load is linearised over the leakflow inlet slot. This procedure takes the hot area prior to the leakflow inlets slot into account while calculating the thermal loads which causes this problem. This error is minimised with sufficiently high resolution but is very prominent for coarser thermal loads. The results from applying these loads are shown in figure 4.14.

Except the general underestimation of the fillet temperature all cases shows obvious differences in the hub thermal profile when changing the number of dimension of the load fields. The most pronounced dependency is of the mixing factor field, or temperature field. This was expected since, as shown, the HTC field only changes marginally when changing reference temperatures while changes in reference temperature affected the metal temperature almost linearly.

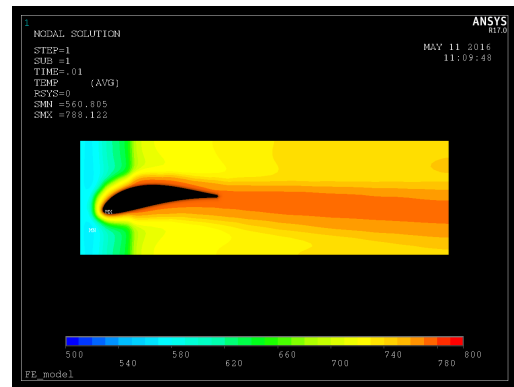
Focusing on the leading edge and the fillet area it can be seen that the increase of resolution improved the predicted profile. The new profile is more smooth which is more realistic and it predicts a higher temperature at the leading edge fillet even if it is still under predicted comparing to the conjugated analysis.

As a comparison to the CFD based HTC, the Frössling correlation described in the theory chapter was used on the leading edge. These results are presented in figure 4.15

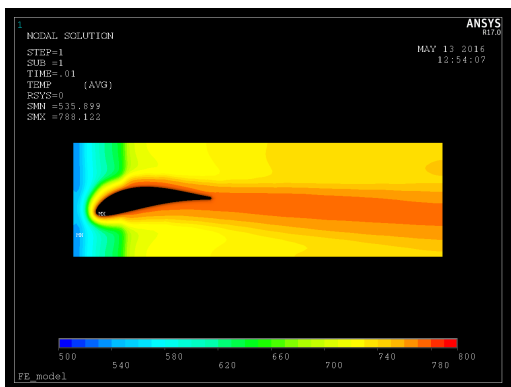
4. Results



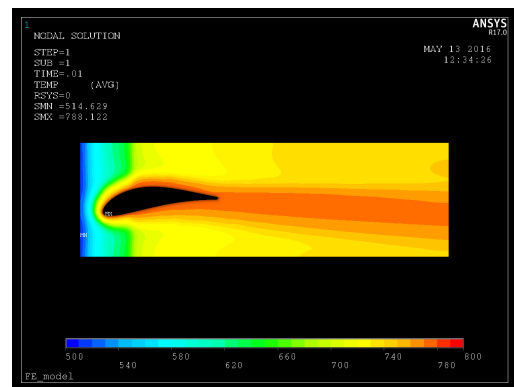
(a) 20x20 elements



(b) 40x40 elements



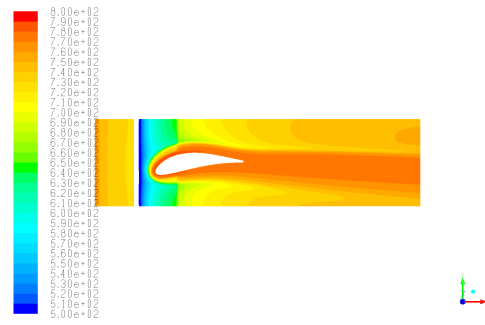
(c) 80x80 elements



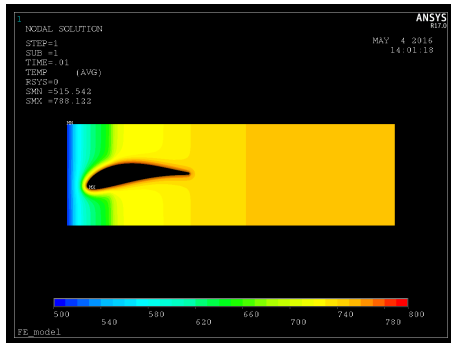
(d) 200x200 elements

Figure 4.14: Resolution effect investigation of the loads applied to the hub surface. Blade thermal loads are kept at 1D.

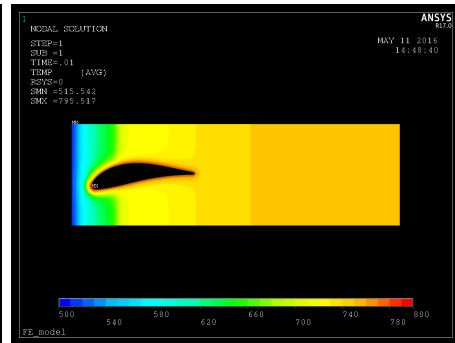
Looking at absolute values, the maximum leading edge temperature using the Frössling correlation can be found to be 794 K compared to the conjugated results of 789 K . Without the correlation the temperature instead becomes 784 K . Frössling overestimates the maximum temperature with 5 K while not using it gives an underestimated result with 5 K . The effect of Frössling is also slightly shifted towards the pressure side compared to the conjugated analysis, and it can be seen in figure 4.15 that its effect on the hub temperature profile is limited to a very small area. The Frössling correlation predicts a HTC fields which is significantly higher than the one predicted using CFD. Since the correlation is based on measurements this could mean that our CFD underestimates the heat transfer coefficient.



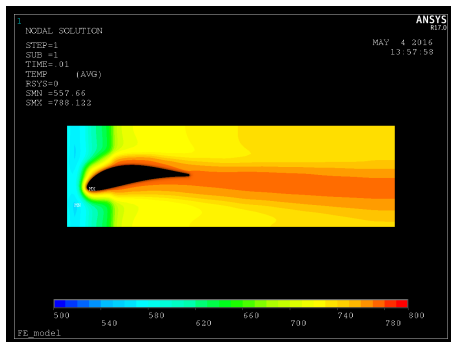
(a) Conjugated analysis



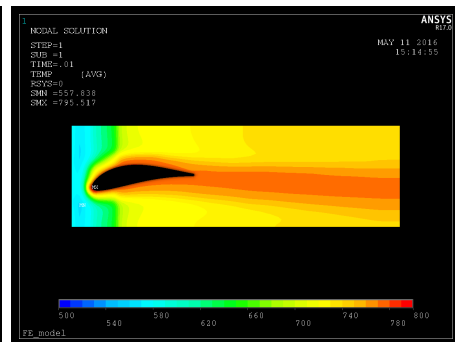
(b) 1D fields



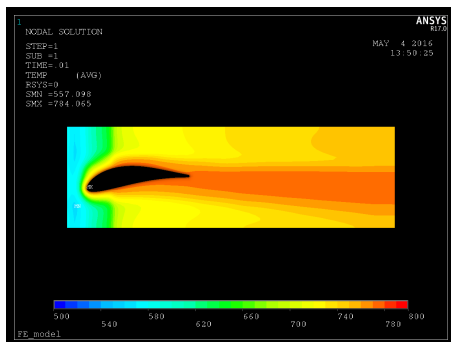
(c) 1D fields, Frössling



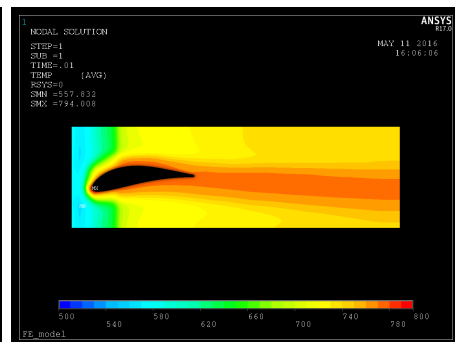
(d) 1D blade, 2D hub



(e) 1D blade, 2D hub, Frössling



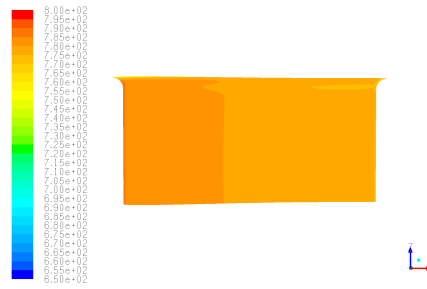
(f) 2D fields



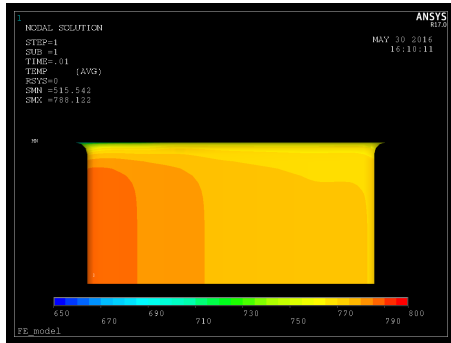
(g) 2D fields, Frössling

Figure 4.15: Effect of applying the Frössling correlation to the leading edge

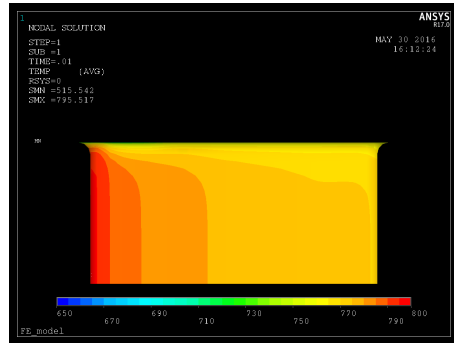
4. Results



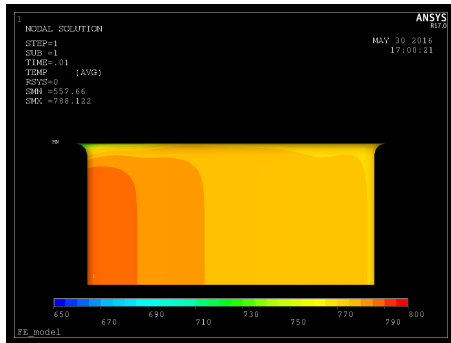
(a) Conjugated analysis



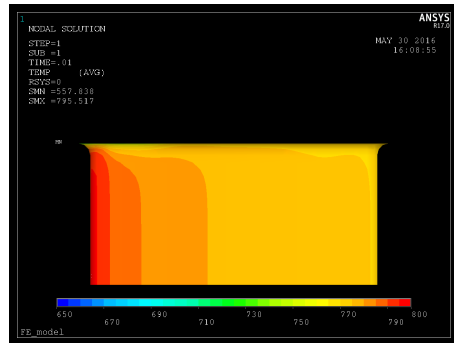
(b) 1D fields



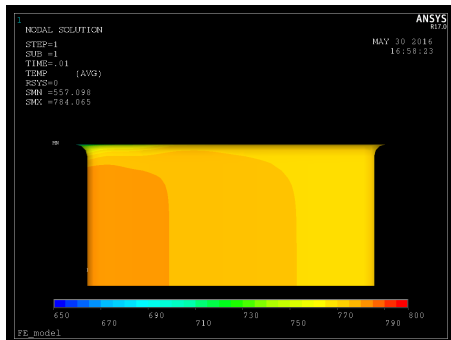
(c) 1D fields, Frössling



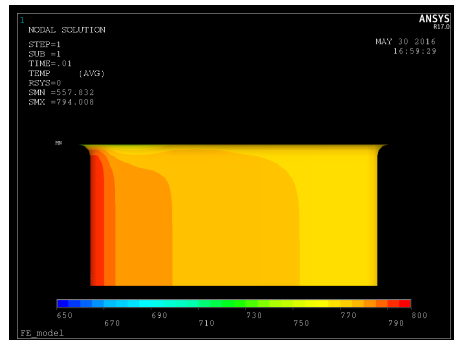
(d) 1D blade, 2D hub



(e) 1D blade, 2D hub, Frössling

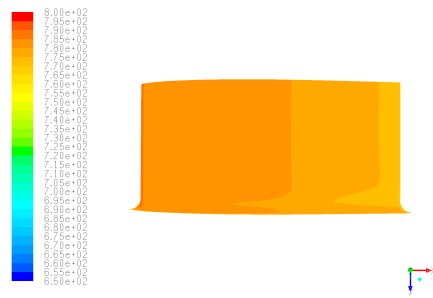


(f) 2D fields

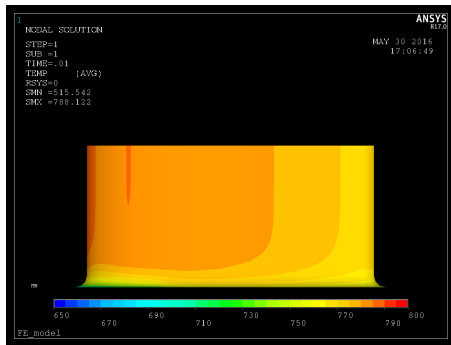


(g) 2D fields, Frössling

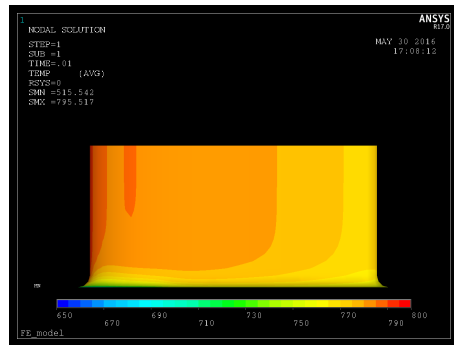
Figure 4.16: Effect of applying the Frössling correlation to the leading edge, pressure side



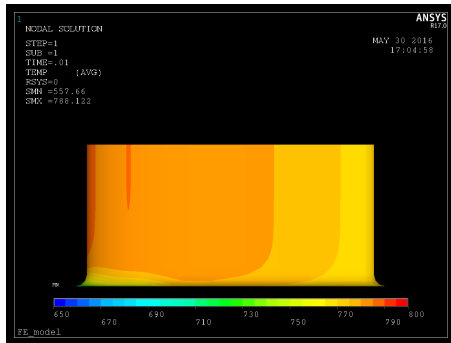
(a) Conjugated analysis



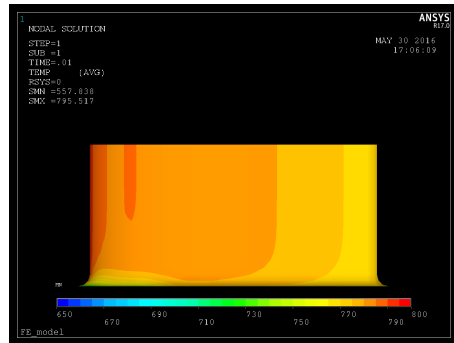
(b) 1D fields



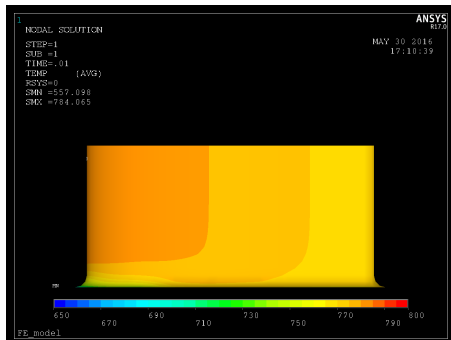
(c) 1D fields, Frössling



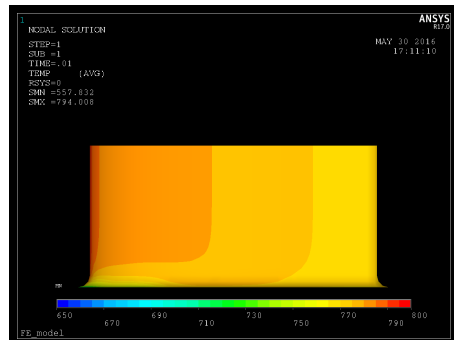
(d) 1D blade, 2D hub



(e) 1D blade, 2D hub, Frössling



(f) 2D fields



(g) 2D fields, Frössling

Figure 4.17: Effect of applying the Frössling correlation to the leading edge, suction side

4.2.4 Real case

The results from the real component shows that it may be essential also on cylindrical structures to take the 2D effects into account. Figure 4.18 shows the temperature profiles on the hub surface using 1D and 2D fields for the mixing coefficient since this was the most important coefficient to resolve. The vane geometry and the scales are confidential information and is therefore omitted in these figures. As for the cascade geometry the 2D thermal load is able to resolve the hot wake area and it also predicts a higher temperature close to the leading edge which was showed to be closer to the reality. Overall the 2D thermal loads gives a temperature profile with a significantly more two dimensional behavior than the one predicted using 1D thermal loads.

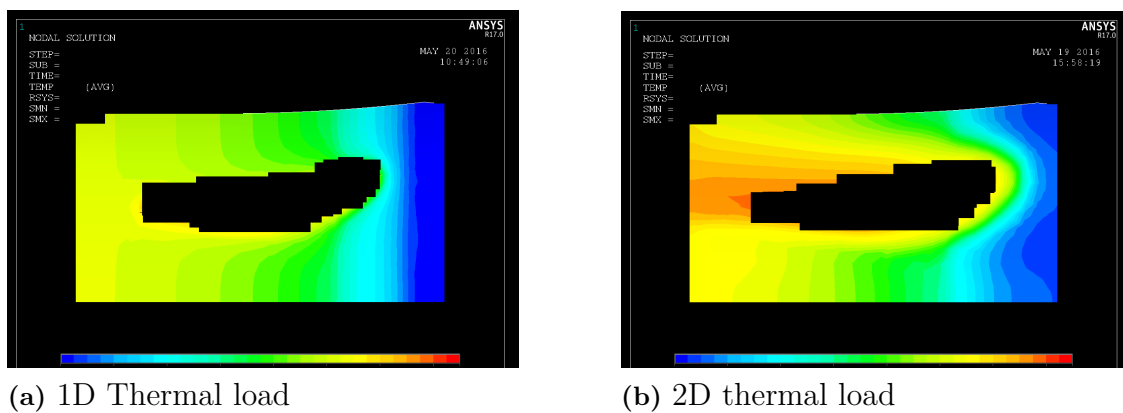


Figure 4.18: Contours of wall temperature using 1D and 2D thermal loads

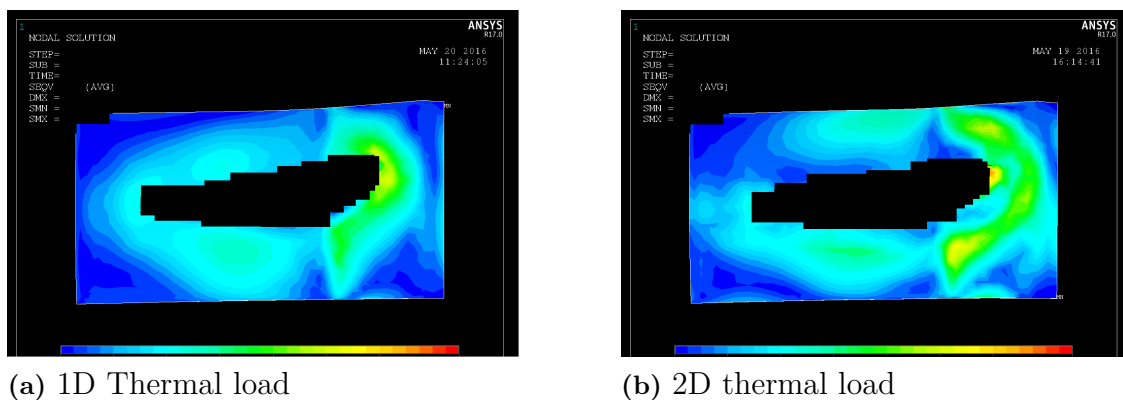


Figure 4.19: Contours of von Mises Stresses using 1D and 2D thermal loads

The results from the stress simulation shown in figure 4.19 displays clear differences between the cases. The 2D thermal load case predicts that the stresses will be concentrated to a few areas of higher stress while the 1D thermal load case predicts a more smooth stress profile. To clarify the scale of the differences in the results three points were chosen from critical areas which were compared. The results are shown in table 4.2

| | 1D | 2D | Difference |
|--------------------------|----|----|------------|
| Leading edge welding | X | X | -27.4% |
| Leading edge hub surface | X | X | +52.12% |
| axial edge welding | X | X | +23.91% |

Table 4.2: Point values taken at critical positions on the vane and hub surfaces

With differences in stress levels with up to over 50% these two cases would give a large difference in expected life time of the component.

5

Conclusion

The results from the initial 2D case shows the influence of unideal breaking of fluid at the wall surfaces reducing the effective temperature below the one expected from an ideal case. This lower temperature, the adiabatic wall temperature, can be approximated using equations 4.5 and available fluid properties with good precision. The results in figure 4.4 shows that using the adiabatic wall temperature improves the resulting wall temperature with $5 K$, leading to a temperature prediction deviation from the conjugated reference case by less than $1 K$. Based on these results the use of the adiabatic temperature as reference temperature should be the obvious choice.

In the hub-film case, the adiabatic temperature is included through the mixing coefficient taken from an adiabatic simulation. In this case the results show that a 2D thermal load is able to resolve the effects of the horseshoe vortex in a much higher degree than the one dimensional thermal load. The resolution proved to affect the results up to a resolution of a node every $2 cm$. Further refinements dramatically increased calculations times but did not alter the results significantly. The stress simulation on the real turbine rear structure shows that the stress levels could differ as much as 50% locally between using 1D and 2D thermal loads, which will give a clear effect on the structural life of the component. With this as a background the recommendation is to keep developing the method using 2D thermal loads.

The Frössling correlation shows that the HTC's resulting from the CFD simulations could be underestimated. A higher HTC would result in higher vane temperature at leading edge which would increase the stresses for both the 1D and the 2D case. Since stress level increases would be expected for both cases this is not expected to have an effect on the conclusions of this thesis.

5.1 Future work

Future work should focus on to make *BCgen_2D_mapping* faster for higher resolutions. It should also be possible to use non symmetrical matrices to be able to chose an appropriate resolution in every directions. An averaging radius was included in the code to calculate a mean value of all CFD nodes within this radius from the thermal load node to define its value. This radius was found to have little effect and might therefore be exchanged to another method to enhance speed.

Often when performing simulations on components the simulation are done over a segment including a single vane as in this project. The same geometry can be divided into computational segments in many ways and this proved to be a source

of error in this project when the CFD and the FE geometries were cut differently. For the real geometry, the CFD mesh was cut in a curved way which introduced a distortion of the thermal load when *BCgen2D_mmapping* extrapolated the values from the CFD simulation to fit the rectangular FE geometry. This extrapolation procedure has to be improved to ensure that no unphysical loads are applied.

The problems with a linearisation of the thermal load over the leak flow inlet slot is usually not a problem due to a different cutting of the surfaces but similar effects could be expected in other holes in the surfaces such as the one created by the vane in the hub surface. This problem should be investigated further. The code should also be adapted to be able to write larger fields as was done during this project to test higher resolutions. Effort should also be put into automating the procedure and simplifying the process of using *BCgen2* and *BCgen_2D_mapping* together to produce mixtures of 1D and 2D fields. Lastly, it would be interesting to investigate the transient performance of the codes.

Bibliography

- [1] Andersson B., Andersson R., Håkansson L., Mortensen M., Sudiyo R. and van Wachem B. (2015) Computational Fluid Dynamics for Engineers (11th). Cambridge University Press.
- [2] Asadzadeh M. (2010). An Introduction to the Finite Element Methods for Differential Equations. Part 1: Problems in 1-D.
- [3] AZo Materials, Information taken 2016-05-31, <http://www.azom.com/article.aspx?ArticleID=4461>
- [4] CFD-Online, Information taken 2016-05-31, http://www.cfd-online.com/Wiki/Best_practice_guidelines_for_turbomachinery_CFD#Turbulence_inlet_conditions
- [5] Frössling N., (1958) Evaporation, Heat Transfer, and Velocity Distribution in Two-Dimensional and Rotationally Symmetrical Laminar Boundary-Layer Flow, NACA, TM 1432
- [6] Kreith F., (1973) Principles of heat transfer (3rd)
- [7] Larson M.G., Bengzon F (2009). the Finite Element Method: theory, Implementation, and Practice. Springer.
- [8] Mörtstedt S.E., Hellsten G. (2010) Data och Diagram, Energi- och kemitekniska tabeller (7th). Liber. ISBN: 978-91-47-00805-6
- [9] Pentenrieder B., (2005) Finite Element Solutions of Heat Conduction Problems in Complicated 3D Geometries Using the Multigrid Method, Technical University of Munich
- [10] Praisner T.J., Smith C.R. (2005). The Dynamics of the horseshoe vortex and associated endwall heat transfer, Part 2 - Time-mean results, GT2005-69091, Proceedings of GT2005, ASME Turbo Expo 2005: Power for Land, Sea and Air.
- [11] Saravanamuttoo H.I.H., Rogers G.F.C., Cohen H. and Straznicky P.V., (2009). Gas Turbine Theory (6th). Pearson Education Limited, ISBN: 978-0-13-222437-6
- [12] SAS IP, Inc., Fluent, User's guide (Release 16.2)
- [13] Schlichting H. (1979) Boundary-Layer Theory (7th). McGraw-Hill. ISBN: 0-07-055334-3
- [14] Versteeg H.K., Malalasekera W., (2007). An Introduction to Computational Fluid Dynamics - The Finite Volume Method (2nd). Pearson Education Limited. ISBN: 978-0-13-127498-3
- [15] Welty J.R., Wicks C.E., Wilson R.E. and Rorrer G.L., (2008) Fundamentals of Momentum, Heat, and Mass Transfer (5th) John Wiley & Sons, Inc. ISBN: 978-0470128688

- [16] Zixiang S., Chew J.W. and Hills N.J., Thermo-Fluid Systems UTC, School of Engineering, University of Surrey, Use of CFD for Thermal Coupling in Aero-engine Internal Air Systems Applications, The 4th International Symposium on Fluid Machinery and Fluid Engineering, November 24-27, 2008, Beijing, China

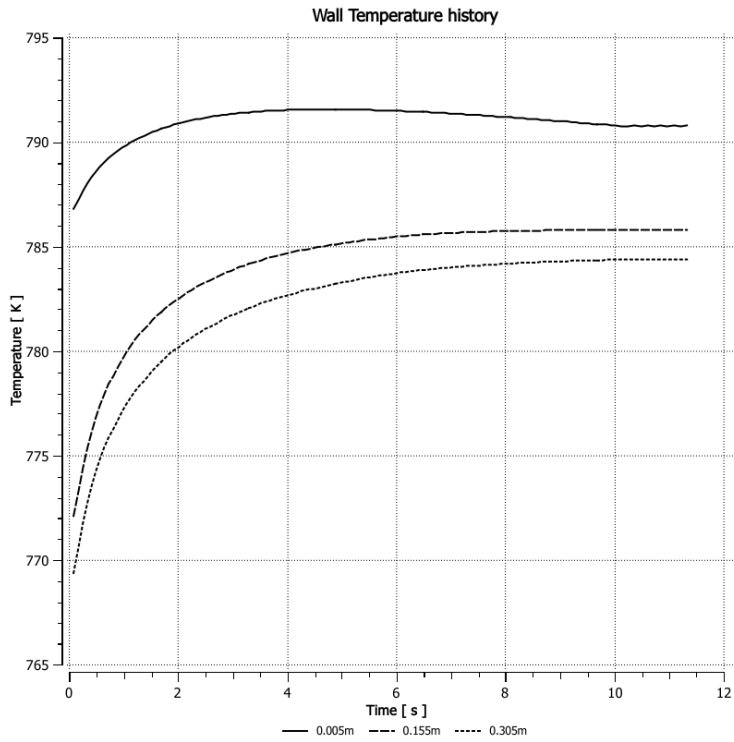
A

Appendix 1 - Transient simulations

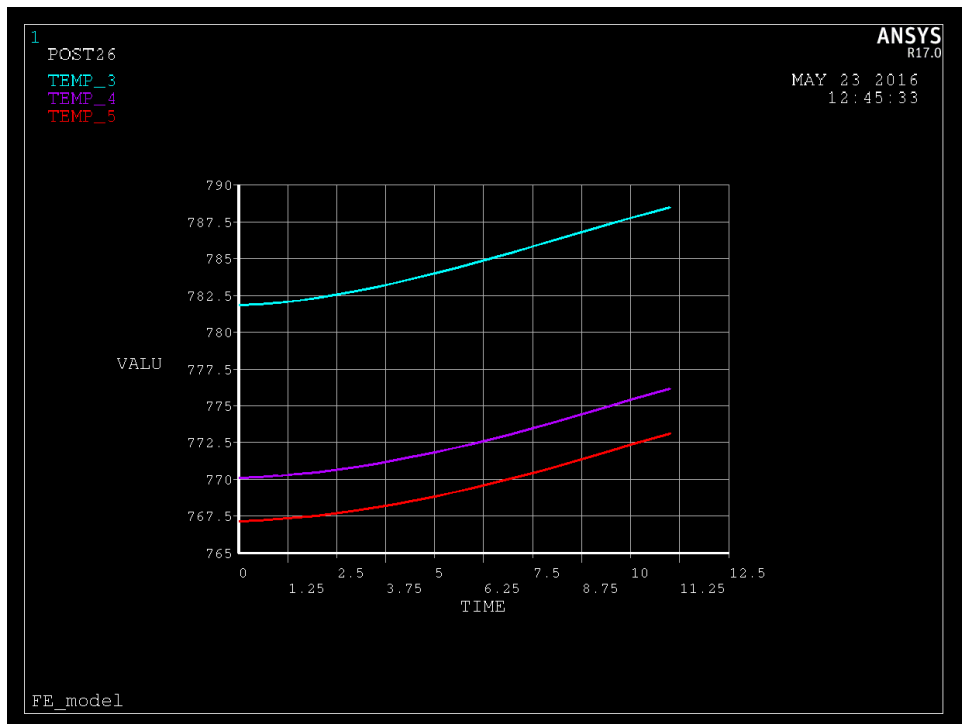
To examine the ability of BCgen2 to simulate a change of working point a transient case was created. This case included a change from idle to take of power at ground level and the effect on the thermal profile of the wall was examined. The mass inlet boundary conditions was changed to a pressure inlet condition resulting in the same mass flow to enhance stability and make the behaviour of the system more realistic. To isolate the effects of the temperature increase and the pressure increase two different cases were created; one with a linear increase of pressure over ten seconds and one with a temperature increase described by

$$T_{tot} = 800 + 40 * (1 - e^{-\alpha(time-a)}) \quad (A.1)$$

where α is a coefficient set to 0.2 and a is the time of running point change. For both these cases the performance of BCgen2 using the correlation was compared to the results from transient conjugated CFD using the same formula for pressure and temperature increase as in BCgen2 applied through a user defined function (UDF). The results are presented in figure A.1 and A.2 and as can be seen was the trend very different in conjugated CFD and one way coupled CFD-FE. Due to time restrictions no further investigation of these results where done in this project and hence it is left for future work.

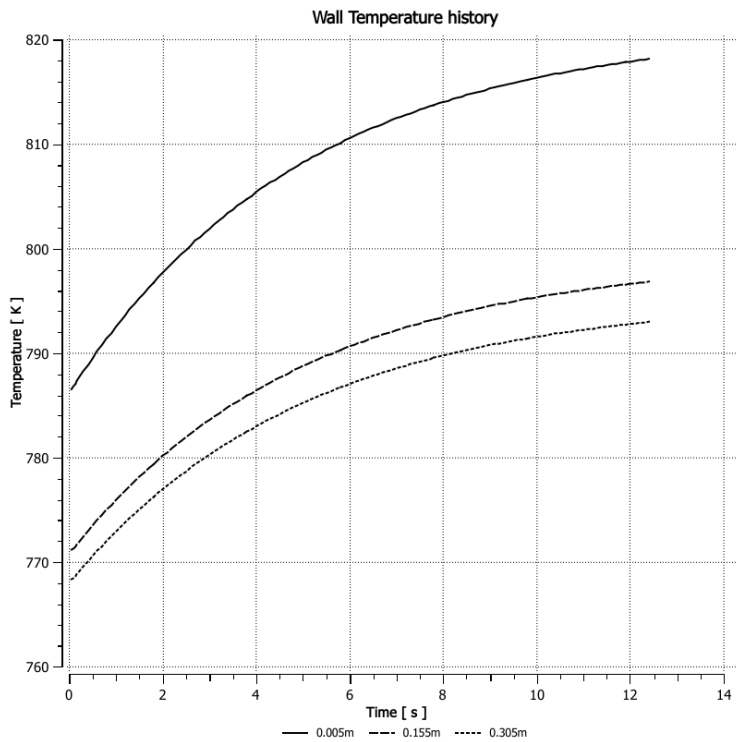


(a) Conjugated CFD

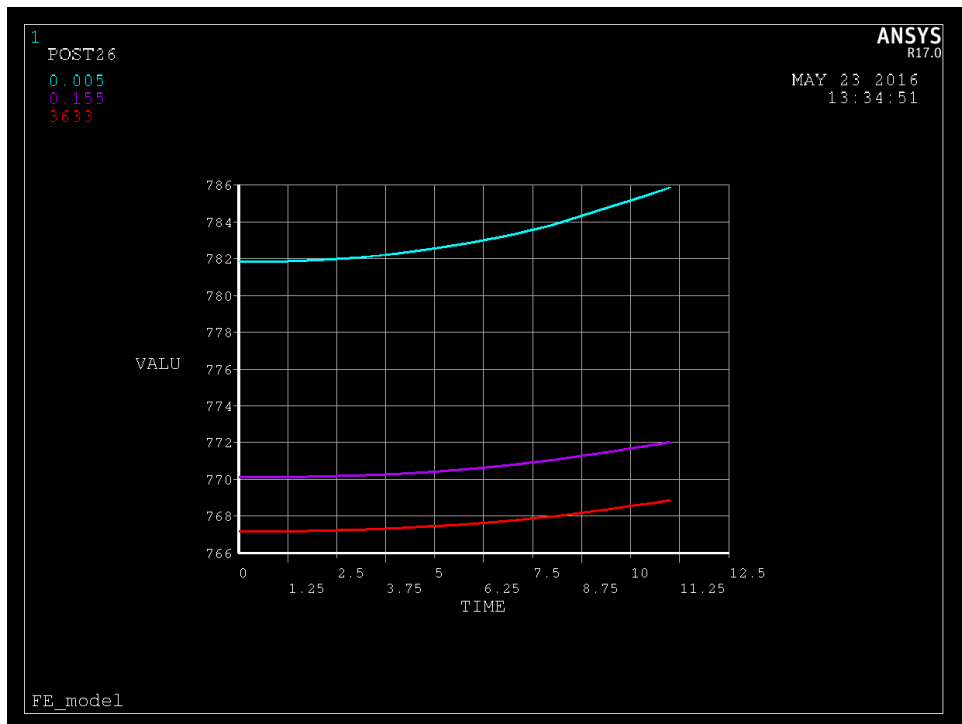


(b) One way coupled CFD-FE

Figure A.1: Wall temperature response to a linear total gauge pressure increase from 604 Pa to 1680 Pa over 10 seconds starting at time 0.01 s. Values are shown for three points on the wall surface.



(a) Conjugated CFD



(b) One way coupled CFD-FE

Figure A.2: Wall temperature response to a total temperature increase from 800 K to 840 over 10 seconds starting at time 0.01 s. Values are shown for three points on the wall surface.